

Heat-Mode Excitation in a Proximity Superconductor

A.O. Denisov,^{1,2} A.V. Bubis,^{3,1} S.U. Piatrusha,¹ N.A. Titova,⁴ A.G. Nasibulin,³
J. Becker,⁵ J. Treu,⁵ D. Ruhstorfer,⁵ G. Koblmüller,⁵ E.S. Tikhonov,¹ and V.S. Khrapai^{1,6}

¹*Osipyan Institute of Solid State Physics,*

Russian Academy of Sciences, 142432 Chernogolovka, Russia

²*Department of Physics, Princeton University,*

Princeton, New Jersey 08544, USA

³*Skolkovo Institute of Science and Technology,*

Nobel street 3, 121205 Moscow, Russian Federation

⁴*Moscow Pedagogical State University,*

29 Malaya Pirogovskaya St, 119435 Moscow, Russia

⁵*Walter Schottky Institut, Physik Department,*

and Center for Nanotechnology and Nanomaterials,

Technische Universität München, Am Coulombwall 4, Garching 85748, Germany

⁶*National Research University Higher School of Economics,*

20 Myasnitskaya Street, 101000 Moscow, Russia

Abstract

Mesoscopic superconductivity deals with various quasiparticle excitation modes, only one of them—the charge-mode—being directly accessible for conductance measurements due to the imbalance in populations of quasi-electron and quasihole excitation branches. Other modes carrying heat or even spin, valley etc. currents populate the branches equally and are charge-neutral, which makes them much harder to control. This noticeable gap in the experimental studies of mesoscopic non-equilibrium superconductivity can be filled by going beyond the conventional DC transport measurements and exploiting spontaneous current fluctuations. Here, we perform such an experiment and investigate the transport of heat in an open hybrid device based on a superconductor proximitized InAs nanowire. Using shot noise measurements, we investigate sub-gap Andreev heat guiding along the superconducting interface and fully characterize it in terms of the thermal conductance on the order of $G_{\text{th}} \sim e^2/h$, tunable by a back gate voltage. Understanding of the heat-mode also uncovers its implicit signatures in the non-local charge transport. Our experiments open a direct pathway to probe generic charge-neutral excitations in superconducting hybrids.

Introduction

Conversion of a quasiparticle current to the collective motion of a Cooper pair condensate at the interface of a normal metal and superconductor is known as Andreev reflection (AR) [1]. For quasiparticle energies (ε) below the superconducting gap (Δ) (sub-gap quasiparticles, $|\varepsilon| < \Delta$), AR is fully responsible for the charge transport across the interface. Conservation of both the number of sub-gap quasiparticles and their excitation energy on the normal side manifests AR as a fundamental example of charge–heat separation in the electronic system. Out of thermal equilibrium, the spatial gradient of a charge-neutral quasiparticle distribution conveys the heat flux [2], which does not penetrate the superconductor and propagates along its boundary with a normal conductor. In this way, ARs mediate the heat conduction via vortex core in s-type superconductors [3] and via neutral modes in graphene [4].

The retro-character of the AR, that is, the propagation of a reflected hole via the time-reversed trajectory of an incident electron, results in a suppression of the heat conduction in the ballistic limit. This obstacle may be overcome by imposing the chirality of the charge carriers in a magnetic field [5–7], similar to quantum Hall-based experiments [8], or by going

in the regime of specular AR near charge-neutrality point in graphene [9]. In the diffusive limit, counter-intuitively, the heat transport is restored, since moderate disorder scattering effectively increases the number of the conducting modes [10]. In addition, the disorder scattering promotes the relaxation of a charge-mode component into pure heat-mode, by mixing the quasi-electron and quasihole branches via AR. For such a relaxation to occur, a superconducting gap has to vary either in momentum space, as in anisotropic bulk superconductors [11], or in real space [12], as in proximity structures, including in the present experiment. All of this makes the geometry of the Andreev wire [10]—a diffusive normal core proximitized by a wrapped around superconductor—preferable for a sub-gap heat transport experiment.

In this work, we challenge a thermal conductance (G_{th}) measurement in an open three-terminal hybrid device based on a diffusive InAs nanowire (NW) proximitized by a superconducting contact, see the image of one of our samples in Figure 1a. Conceptually similar devices were investigated in the context of Cooper-pair splitters [13–15] and, more recently, Majorana physics [16–21] with the emphasis on the electrical conductance. The central part of the device represents a few 100 nm long Andreev wires with a partial superconducting wrap, which removes complications arising from the Little–Parks effect [22, 23]. In a previous work with the same devices [24], we have demonstrated a charge neutrality of a non-local quasiparticle response, which is direct evidence of the heat-mode excitation regime. Here, we focus on a comparison of local and non-local noise signals, evaluation of thermal conductance and the origin of transport signals in this regime. Our experiments offer a so-far missing experimental tool in the field of non-equilibrium mesoscopic superconductivity [25–30] and enable the control of generic charge-neutral excitations in superconducting hybrids.

Results: Devices and Transport Response

The outline of our experiment is depicted in Figure 1b. A semiconducting InAs nanowire is equipped with a superconducting (S) terminal, made of Al, in the middle and two normal metal (N) terminals, made of Ti/Au bilayer, on the sides. Below, we focus on the data from two devices. In the device NSN-I (NSN-II), the length of the NW underneath the superconductor is 200 nm (300 nm) and the NW segments between the S-terminal and the N-terminals are 350 nm (300 nm) long. In essence, this device layout represents two back-to-back normal metal–NW–superconductor (NS) junctions sharing the same S-terminal. Note

the absence of the quantum dots [13, 15, 19] or tunnel barriers [18] adjacent to the S-terminal, which enables better coupling of the sub-gap states to the normal conducting regions. Throughout the experiment, the S-terminal is grounded, terminal N1 is biased and terminal N2 is floating (or vice versa). Note that grounding of the S-terminal protects the Al from non-equilibrium superconductivity effects [25, 31]. The S-terminal serves as a nearly perfect sink for the charge current. At energies below the superconducting gap $\Delta \approx 180 \mu\text{eV}$ of Al, the S-terminal cannot absorb quasiparticles [1] and their non-equilibrium population can relax only via diffusion to the N terminals [32], manifesting charge-heat separation. This charge-neutral diffusion flux, which is referred to as the heat flux below, is shown by curly arrows in Figure 1b. One part of the heat flux relaxes via the biased terminal, similar to the usual two-terminal configurations [33, 34]. The other part bypasses the S-terminal and relaxes via floating terminal. As we will demonstrate below, this heat flux can be detected by means of shot noise thermometry.

For charge-heat separation via AR, the quality of the InAs/Al interface is important, which we verify in transport measurements. In Figure 1c, we show the local differential conductance G_2 of the biased junction N2-S in device NSN-II as a function of voltage V_2 at a temperature $T = 50 \text{ mK}$. Without the magnetic field (B), G_2 exhibits two well-defined maxima at finite V_2 that diminish with increasing the B -field directed perpendicular to the substrate and vanish in $B \approx 20 \text{ mT}$ simultaneously with the transition of the Al to the normal state. The maxima occur around gap edges $V_2 = \pm\Delta/|e|$, where e is the elementary charge, and the corresponding increase of G_2 above the normal state value reaches about 15%. This re-entrant conductance behavior is a property of diffusive NS junctions with a highly transparent interface [35]. Around zero bias in $B = 0$, we generally observed a small reduction of G_2 by about 10% in all back gate voltage (V_g) range studied. This guarantees that possible residual reflectivity has a minor effect and ARs dominate over normal interface scattering in our devices.

In Figure 1d, we plot non-local differential resistance $r_{21} = dV_2/dI_1$, where V_2 is the voltage on terminal N2, as a function of V_1 . In the normal state r_{21} is featureless and consists of the interface resistance along with a few-Ohm contribution of the Al lead, see the trace in $B = 50 \text{ mT}$ in device NSN-I with $r_{21} \approx 40 \Omega$. By contrast, in $B = 0$ strong gap-related features develop and r_{21} demonstrates local maximum and minima at the gap edges, see vertical arrows. Note that $B = 0$ behavior is non-universal and depending on V_g ,

we have also observed bias asymmetry and sign reversal of the r_{21} , see two lower datasets for the device NSN-II. These features are related to the energy dependence of the sub-gap conductance and have a thermoelectric-like origin [36], as will be discussed below. Overall, r_{21} being small compared to the individual resistances of the NS junctions signals that the current transfer length l_T is small compared with the width of the S-terminal. We estimate $l_T \leq 100$ nm close to the superconducting coherence length in Al, which sets the lowest possible bound for the l_T , see Supplemental Materials for the details. r_{21} can be expressed via a non-diagonal element of the conductance matrix [37] as $r_{21} \approx -G_{21}/G_2G_1$, where $G_i \approx G_{ii}$ ($i = 1, 2$) are the two-terminal conductances of the NS junctions. $G_{21} \sim 10^{-2}G_i$ is a direct consequence of a charge-neutrality of the non-local response in our devices [24] and proves nearly perfect efficiency of the S contact as charge current sink. The actual sign of the non-local conductance G_{21} can be both negative and positive, as determined by a competition of normal and Andreev transmission processes. Corresponding non-local transmission probabilities are commonly denoted by T_{21}^{ee} and T_{21}^{he} , respectively [38]. In the present experiment, at zero bias, we observe a small negative conductance $G_{21} < 0$, implying that $\Sigma T_{21}^{ee} > \Sigma T_{21}^{he}$, where sum is performed over the eigenchannels.

Results: Shot Noise Response

Next, we probe the non-equilibrium electronic populations in both NS junctions using shot noise current fluctuations picked-up in the reflection and transmission configurations sketched in Figure 1b. This measurement is performed using a schematics based on a resonant tank circuit and a home-made low-temperature amplifier. The measurement layout and the calibration procedure are detailed in the Supplemental Materials. Figure 2a demonstrates the noise spectral density measured in terminal N2 as a function of I_2 at two gate voltages. This configuration, referred to as the reflection configuration, is reminiscent of the usual AR noise in two-terminal devices [33, 34], and the measured noise is denoted as S_R . Experimentally, S_R represents the spectral density of the auto-correlation noise of current I_2 under the bias applied to the terminal N2, while the terminal N1 is maintained DC floating, that is, $S_R \equiv S_{22}(I_1 = 0, I_2)$. The corresponding experimental layout is depicted in the left sketch of Figure 1b. For comparison, a similar measurement in a reference NS device is shown in Figure 2c. In both devices, the results are qualitatively similar, that is, the S_R

scales linearly with current and exhibits clear kinks at the gap edges (marked by the arrows). Above the kinks, the diminished slope is the same and it corresponds closely to the universal Fano factor $F \equiv 1/3$ in a diffusive conductor with normal leads [39, 40] $\delta S_R/2e\delta I \approx F$, as shown by the dashed lines with a marker “ e ”. This familiar behavior [15] verifies elastic diffusive transport in InAs NWs [41] even at energies well above Δ and ensures quasiparticle relaxation solely by diffusion in contacts. In particular, this observation establishes a solid correspondence between the applied bias voltage and the quasiparticle excitation energy in the present experiment. Namely, a small bias window of $[V; V + dV]$ corresponds to a creation of electron-like and hole-like quasiparticles with the excess energy of $|\varepsilon| = |eV|$. At sub-gap biases ($|V| < \Delta/|e|$), we observe an important difference being a result of joining an extra N-terminal. While in the NS device the slope expectedly doubles [15, 33], see the dotted lines in Figure 2c with the effective charge $e^* \approx 2e$ denoted by “ $2e$ ”, in the NSN device, it increases much more weakly and corresponds to $e^* \approx 1.6e$ assuming the same F . Unlike in SNS junctions [42], a fractional value of e^* here is not related to a quasiparticle charge in the superconductor, but reflects an unusual boundary condition for the heat flux underneath the S-terminal, see Ref. [31] and Supplemental Materials for the details. While the doubled e^* is a direct consequence of the full reflection of heat flux at the S-terminal [32], its intermediate value means that the missing heat flux in the NSN device is transmitted towards the nearby floating N-terminal. Similar behavior was previously observed in topological insulators [43], however, in the present experiment, the transmitted heat flux is directly measurable, as we show below.

In Figure 2b, we plot the current dependencies of the shot noise measured in transmission configuration, S_T , that is, the noise at the floating terminal N2. In this configuration, we measure the auto-correlation noise at the DC floating terminal N2 under a finite bias current I_1 , that is, $S_T \equiv S_{22}(I_1, I_2 = 0)$. The corresponding experimental layout is depicted in the right sketch of Figure 1b. Within all investigated V_g range, S_T steeply increases at small currents followed by pronounced kinks at the gap edges, see the arrows for some of the traces, and keeps increasing much more weakly above the kinks. This behavior of S_T is explained as follows. Sub-gap quasiparticles diffusing along the superconductor, and experiencing a few ARs on the way, guide the heat flux via proximitized InAs. Above-gap quasiparticles, however, mostly leave via the S-terminal and their contribution to the transmitted heat signal is minimal. This qualitative picture is proved in the following crosscheck experiment.

In the upper part of Figure 2b, the S_T signals are compared in $B = 0$ and $B = 50$ mT with the Al in superconducting and normal states, respectively. In the normal state, S_T grows weakly at increasing I_1 without any kinks. Moreover above-gap signal in $B = 0$ roughly reproduces this trend up to a vertical shift at high I_1 . We conclude that this effect is mainly caused by residual normal interface scattering, see also Ref. [24]. Importantly, for sub-gap energies, $S_T \sim S_R$, cf. Figure 2a, whereas non-local charge transport resulted in $|G_{21}| \ll G_1, G_2$. This difference emphasizes the fact that non-equilibrium populations of quasiholes and quasi-electrons are balanced in the proximity region and transmitted noise directly probes the heat-mode excitation. Figure 2b, therefore, demonstrates our main result that at sub-gap energies the proximitized InAs NW supports guiding of heat underneath the S-terminal by virtue of AR processes.

We proceed with a quantitative description of the Andreev heat guiding by solving the diffusion equation for the electronic energy distribution (EED), inspired by a quasiclassical approach [31, 32]. In the proximitized region, the boundary conditions take into account ARs for the sub-gap transport and residual normal reflections above the gap. Thermal conductance G_{th} and interface resistance r are the only two parameters that, together with known G_1 , G_2 , determine the solution for the EED and the noise temperature T_N of the floating NS junction [44]. For convenience, we choose electrical units for the thermal conductance [31] $G_{\text{th}} = e^2 \nu^* D^* / L_S$, where ν^* is the effective one-dimensional density of states, D^* is the diffusion coefficient in the NW region covered by the superconductor and L_S is the length of the S-terminal. With this choice, in case of energy-independent G_{th} , one can express the heat flux caused by a small thermal bias δT applied across the proximity region as $\dot{Q} = G_{\text{th}} \mathcal{L}_0 T \delta T$, where $\mathcal{L}_0 = \pi^2 k_B^2 / 3e^2$ is the Lorenz number. The details of theoretical modeling can be found in the Supplemental Materials. In Figure 3a, we compare the T_N measured in the experiment of Figure 2b (solid lines) with the model fits (dashed lines), where $T_N \equiv S_T / 4k_B G_2$. Plotted as a function of V_1 the kinks in T_N indeed occur at the gap edges for all V_g values, see the vertical arrows. The data are perfectly reproduced, ensuring that our model captures correctly the physics of the Andreev heat guiding effect. The V_g dependence of the interface parameter r is shown in Figure 3c. We find $r \sim 50 \Omega$, which is consistent with r_{21} in the same device in the normal state, cf. Figure 1d, and almost independent of V_g . The evolution of G_{th} at increasing V_g is shown by symbols in Figure 3b. The initial growth is followed by saturation at $G_{\text{th}} \sim 2e^2/h$. This is in contrast with a mono-

tonic increase of the electrical conductances G_1 , G_2 of NS junctions in the same device, see the lines in Figure 3b. We attribute this difference to the impact of superconducting proximity effect that diminishes the density of states stronger at higher carrier densities. Note that while the back-gate sensitivity of G_{th} is consistent with the behavior of the sub-gap states in the NW region covered on top by the superconductor [45], the microscopic origin of such states and its possible relation, e.g., to the spin-orbit coupling in InAs, goes beyond the scope of the present experiment.

Results: Non-Equilibrium DC Transport

So far, we have used shot noise measurements to demonstrate sub-gap Andreev heat guiding. In the following, we concentrate on the signatures of this effect in charge transport measurements in the device NSN-II. First, we focus on resistive thermometry based on a weak T -dependence of the mesoscopic conductance fluctuations. In Figure 4a we plot the out-of-equilibrium linear response resistance $R_1 = \partial V_1 / \partial I_1|_{I_1=0, I_2 \neq 0}$ of the floating NS junction as a function of V_2 (see the upper sketch in Figure 4 for the measurement configuration). R_1 exhibits the same qualitative behavior as the S_T before, with much stronger dependence at sub-gap energies, kinks at the gap edges and suppression in B -field. Using the equilibrium dependencies $R_1(T)$ for calibration, we converted these data in the effective temperature T^* of the floating NS junction and plotted in Figure 4b. The behavior of T^* is similar to that of the T_N in the device NSN-I, cf. Figure 3a, potentially making this approach an alternative for the detection of transmitted heat fluxes. Note, however, that resistive thermometry slightly underestimates the effect compared to a simultaneously measured T_N , see Supplemental Materials for the details of the analysis. This may be a result of dephasing that causes averaging of the conductance fluctuations and was not taken into account.

Finally, we investigate non-local I - V characteristics in the configuration shown in the lower sketch of Figure 4. In Figure 4c, the voltage V_2 is plotted as a function of I_1 for three representative values of V_g . All traces lack full antisymmetry, $V_2(I_1) \neq -V_2(-I_1)$, moreover, the lower and upper traces exhibit local extrema near the origin, meaning that here the symmetric component dominates the I - V . This is a signature of the Andreev rectification effect [37], which also caused the asymmetry and sign reversal of r_{21} in Figure 1d. Figure 4d shows the symmetric component of the non-local voltage $V_2^{\text{symm}} \equiv [V_2(I_1) + V_2(-I_1)]/2$

against V_1 . V_2^{symm} evolves concurrently to the T^* and T_N with pronounced sub-gap behavior and kinks at $V_1 \approx \pm\Delta/e$, see vertical arrows. The signal is small, in 1 μV range, with both the sign and magnitude demonstrating strong V_g -dependent fluctuations, in contrast with T^* and T_N . We suggest that the finite V_2^{symm} has a thermoelectric-like origin, analogous to thermopower in Andreev interferometers [36], and results from the thermal gradient that builds up in response to the transmitted heat flux. More rigorously, in the absence of inelastic processes in the present experiment, one should think in terms of a spatial gradient of a non-equilibrium EED [31]. The data in Figure 4d are consistent with V_g fluctuations of the Seebeck coefficient in InAs NWs without superconductors [46, 47] in the range $|S/T| \sim 5 \mu\text{V}/\text{K}^2$, corresponding fits shown by the dashed lines (see Supplemental Materials for the details). In the present experiment, thermoelectric-like response also comes from the energy dependence of the mesoscopic fluctuations, but it can be additionally affected by the Andreev scattering [37]. Note that the degree of asymmetry of the non-local conductance $G_{21} \propto -(dV_2/dI_1)$ caused by this effect (see Figure 1d) is comparable to the data in a Cooper pair splitter [48] and in a tunnel-coupled Majorana device [49, 50]. Our thermoelectric interpretation may also be useful in explaining these data.

Discussion

Our experiment reveals the heat-mode excitation in a proximity superconductor via different experimental signatures. On the one hand, in DC transport, both in the resistive thermometry (Figure 4a,b) and in the non-local Andreev rectification (Figure 4d), the heat-mode non-equilibrium manifests itself through the energy dependence of sub-gap quasiparticle transmission probabilities. These energy dependencies are encoded in the T -dependence of the linear-response diagonal elements of the conductance matrix (see the Supplemental Materials for the details) and in the effective Seebeck coefficient. On the other hand, in shot noise, the energy dependence is irrelevant and the data of Figure 3a are perfectly fitted with the energy-independent G_{th} . This difference between the transport and noise approaches is conceptual and lies in the charge-neutral origin of the heat-mode excitation, earlier discussed in Ref. [24]. Below, we briefly analyze the origin of various non-local responses in the present experiment.

Consider for simplicity the case of a single mode NSN device, for which the non-local

electrical and thermal conductances are given by $G_{21} = G_0 \mathcal{T}_{21}^-$ and $G_{\text{th}} = G_0 \mathcal{T}_{21}^+$, where $G_0 = 2e^2/h$ and $\mathcal{T}_{21}^\pm = T_{21}^{he} \pm T_{21}^{ee}$ denote the sum/difference of the non-local Andreev and normal transmission probabilities. The observation of $G_{\text{th}} \gg G_{21}$ implies a predominance of the heat-mode excitation over the charge-mode, that is $T_{21}^{he} \approx T_{21}^{ee} \gg |\mathcal{T}_{21}^-|$. In this situation, a weak energy dependence of the transmission probabilities primarily affects the G_{21} . Within the first-order expansion $\mathcal{T}_{21}^- = \mathcal{T}_{21}^-(0) + \varepsilon (d\mathcal{T}_{21}^-/d\varepsilon)$, therefore, the non-local $I - V$ characteristics acquire symmetric component. Using the formalism of Ref. [38], we obtain for the configuration of the bottom sketch in Figure 4: $V_2^{\text{symm}} = -|e|(G_0/G_{22}) (d\mathcal{T}_{21}^-/d\varepsilon) (V_1)^2/2$, or, equivalently, $V_2^{\text{symm}} = -|e|(dG_{21}/d\varepsilon)(V_1)^2/2G_{22}$. The latter relation is also valid in the multimode case, bridging the effective Seebeck coefficient with the energy dependence of the spectral conductance. Similarly, the energy dependence of the diagonal conductance $G_{22}(\varepsilon)$ is responsible for the resistive thermometry signal in the configuration of the top sketch in Figure 4. Here, the non-zero term comes from the second derivative $d^2G_{22}/d\varepsilon^2$, as follows from the derivation given in the Supplemental Materials. Such effects are completely irrelevant for the non-local shot noise measurement in the transmission configuration. Estimated from Figure 4d, the energy dependence of the transmission probabilities can result in $\sim 1\%$ variation of the $G_{\text{th}}(\varepsilon)$ within the sub-gap window $|\varepsilon| < \Delta$ in the device NSN-II. Hence, $G_{\text{th}}(\varepsilon) \approx \text{const}$ and the shot noise in the transmission configuration reads $S_{\text{T}} = 2|eV_1|G_{\text{th}}$ (at $T = 0$). Note, however, that the energy-independent G_{th} is puzzling itself and, obviously, contradicts the expected presence of the induced superconducting gap in the proximitized NW region. A microscopic resolution of this puzzle is a difficult theoretical task and goes beyond the scope of the present work.

In summary, we investigated the heat-mode excitation manifesting itself in various non-local responses in NSN proximity devices based on InAs NWs. In DC transport, the non-local signals couple to the heat-mode only indirectly, via a weak and non-universal energy dependence of the spectral conductance. This is in stark contrast with our shot noise approach, which senses the randomness caused by the non-equilibrium EED itself, without the need for any type of spectral resolution [51]. In the same way, the shot noise can also probe excitations of different origin, e.g., spin currents in superconducting spintronics [52], or even valley currents [53], by virtue of spontaneous fluctuations that arise when such currents are fed into the adjacent normal lead [54–57]. Possible applications are not at all limited to the NW-based material platforms. From this perspective, our experiment establishes a natural

background to probe charge-neutral excitations, both above-gap in bulk superconductors and sub-gap in proximity superconductors, including the proposed detection of Majorana zero modes in heat transport [58–62] and, possibly, in measurements of the entanglement entropy [63].

Supplementary. The Supplemental Materials for this article contain Figure S1: Sketch of the experimental setup; Figure S2: Calibration via equilibrium noise; Figure S3: Shot-noise analysis; Figure S4: Additional data in device NSN-I: local conductance; Figure S5: Additional data in device NSN-II: local conductance; Figure S6: Additional data in device NSN-I: non-local conductance; Figure S7: Additional data in device NSN-II: non-local conductance; Figure S8: Effective resistance model for NW/S interface; Figure S9: T-dependence in the linear response regime and calibration of the resistive thermometry; Figure S10: T-dependence beyond the linear response regime; Figure S11: Analytical model: layout and EED; Figure S12: Analytical model: results; Figure S13: Comparison of the non-local noise thermometry and resistive thermometry; Figure S14: Superconducting critical temperature of the Al-film. Supplemental Materials cite References [32, 41, 44, 64–67].

Author Contributions. Shot noise experiments: A.D. and S.P.; transport experiments: A.D., A.B. and S.P.; fabrication: A.B. and N.T.; nanowire growth: J.B., J.T., D.R. and G.K.; modeling: A.D. and S.P.; supervision, writing and project administration: E.T., A.N. and V.K. All authors have read and agreed to the published version of the manuscript.

Funding. Implementation of resistive thermometry and its comparison to noise thermometry was supported by the Russian Science Foundation Grant No. 18-72-10135. Theoretical modeling was performed under the state task of the ISSP RAS.

Data Availability. The full data for this study can be obtained from the corresponding author upon reasonable request.

Acknowledgements. We are grateful to S.M. Frolov, A.P. Higginbotham, T.M. Klapwijk, S. Ludwig, A.S. Mel’nikov and K.E. Nagaev for helpful discussions.

-
- [1] Andreev, A.F. Thermal Conductivity of the Intermediate State of Superconductors. *JETP Lett.* **1964**, *46*, 1823–1828.
 - [2] Giazotto, F.; Heikkilä, T.T.; Luukanen, A.; Savin, A.M.; Pekola, J.P. Opportunities for meso-

- scopics in thermometry and refrigeration: Physics and applications. *Rev. Mod. Phys.* **2006**, *78*, 217–274. <https://doi.org/10.1103/RevModPhys.78.217>.
- [3] Caroli, C.; Gennes, P.D.; Matricon, J. Bound Fermion states on a vortex line in a type II superconductor. *Phys. Lett.* **1964**, *9*, 307–309. [https://doi.org/10.1016/0031-9163\(64\)90375-0](https://doi.org/10.1016/0031-9163(64)90375-0).
- [4] Titov, M.; Ossipov, A.; Beenakker, C.W.J. Excitation gap of a graphene channel with superconducting boundaries. *Phys. Rev. B* **2007**, *75*, 045417. <https://doi.org/10.1103/PhysRevB.75.045417>.
- [5] Lee, G.H.; Huang, K.F.; Efetov, D.K.; Wei, D.S.; Hart, S.; Taniguchi, T.; Watanabe, K.; Yacoby, A.; Kim, P. Inducing superconducting correlation in quantum Hall edge states. *Nat. Phys.* **2017**, *13*, 693–698. <https://doi.org/10.1038/nphys4084>.
- [6] Zhao, L.; Arnault, E.G.; Bondarev, A.; Seredinski, A.; Larson, T.F.Q.; Draelos, A.W.; Li, H.; Watanabe, K.; Taniguchi, T.; Amet, F.; et al. Interference of chiral Andreev edge states. *Nat. Phys.* **2020**, *16*, 862–867. <https://doi.org/10.1038/s41567-020-0898-5>.
- [7] Kurilovich, V.D.; Raines, Z.M.; Glazman, L.I. Disorder in Andreev reflection of a quantum Hall edge. *arXiv* **2022**, arXiv:2201.00273.
- [8] Banerjee, M.; Heiblum, M.; Rosenblatt, A.; Oreg, Y.; Feldman, D.E.; Stern, A.; Umansky, V. Observed quantization of anyonic heat flow. *Nature* **2017**, *545*, 75–79. <https://doi.org/10.1038/nature22052>.
- [9] Beenakker, C.W.J. Specular Andreev Reflection in Graphene. *Phys. Rev. Lett.* **2006**, *97*, 067007. <https://doi.org/10.1103/PhysRevLett.97.067007>.
- [10] Kopnin, N.B.; Mel’nikov, A.S.; Vinokur, V.M. Reentrant localization of single-particle transport in disordered Andreev wires. *Phys. Rev. B* **2004**, *70*, 075310. <https://doi.org/10.1103/PhysRevB.70.075310>.
- [11] Tinkham, M. *Introduction to Superconductivity*; Dover Books on Physics Series; Dover Publications: 2004.
- [12] Artemenko, S.N.; Volkov, A.F. Electric fields and collective oscillations in superconductors. *Sov. Phys. Uspekhi* **1979**, *22*, 295–310. <https://doi.org/10.1070/pu1979v022n05abeh005495>.
- [13] Hofstetter, L.; Csonka, S.; Nygård, J.; Schönenberger, C. Cooper pair splitter realized in a two-quantum-dot Y-junction. *Nature* **2009**, *461*, 960–963. <https://doi.org/10.1038/nature08432>.

- [14] Herrmann, L.G.; Portier, F.; Roche, P.; Yeyati, A.L.; Kontos, T.; Strunk, C. Carbon Nanotubes as Cooper-Pair Beam Splitters. *Phys. Rev. Lett.* **2010**, *104*, 026801. <https://doi.org/10.1103/PhysRevLett.104.026801>.
- [15] Das, A.; Ronen, Y.; Heiblum, M.; Mahalu, D.; Kretinin, A.V.; Shtrikman, H. High-efficiency Cooper pair splitting demonstrated by two-particle conductance resonance and positive noise cross-correlation. *Nat. Commun.* **2012**, *3*, 1165.
- [16] Lutchyn, R.M.; Sau, J.D.; Das Sarma, S. Majorana Fermions and a Topological Phase Transition in Semiconductor-Superconductor Heterostructures. *Phys. Rev. Lett.* **2010**, *105*, 077001. <https://doi.org/10.1103/PhysRevLett.105.077001>.
- [17] Oreg, Y.; Refael, G.; von Oppen, F. Helical Liquids and Majorana Bound States in Quantum Wires. *Phys. Rev. Lett.* **2010**, *105*, 177002. <https://doi.org/10.1103/PhysRevLett.105.177002>.
- [18] Albrecht, S.M.; Higginbotham, A.P.; Madsen, M.; Kuemmeth, F.; Jespersen, T.S.; Nygård, J.; Krogstrup, P.; Marcus, C.M. Exponential protection of zero modes in Majorana islands. *Nature* **2016**, *531*, 206–209. <https://doi.org/10.1038/nature17162>.
- [19] Deng, M.T.; Vaitiekėnas, S.; Hansen, E.B.; Danon, J.; Leijnse, M.; Flensberg, K.; Nygård, J.; Krogstrup, P.; Marcus, C.M. Majorana bound state in a coupled quantum-dot hybrid-nanowire system. *Science* **2016**, *354*, 1557–1562. <https://doi.org/10.1126/science.aaf3961>.
- [20] Yu, P.; Chen, J.; Gomanko, M.; Badawy, G.; Bakkers, E.P.A.M.; Zuo, K.; Mourik, V.; Frolov, S.M. Non-Majorana states yield nearly quantized conductance in proximatized nanowires. *Nat. Phys.* **2021**, *17*, 482–488. <https://doi.org/10.1038/s41567-020-01107-w>.
- [21] Wang, G.; Dvir, T.; van Loo, N.; Mazur, G.P.; Gazibegovic, S.; Badawy, G.; Bakkers, E.P.A.M.; Kouwenhoven, L.P.; de Lange, G. Non-local measurement of quasiparticle distribution in proximitized semiconductor nanowires using quantum dots. *arXiv* **2021**, arXiv:2110.05373.
- [22] Vaitiekėnas, S.; Winkler, G.W.; van Heck, B.; Karzig, T.; Deng, M.T.; Flensberg, K.; Glazman, L.I.; Nayak, C.; Krogstrup, P.; Lutchyn, R.M.; et al. Flux-induced topological superconductivity in full-shell nanowires. *Science* **2020**, *367*, eaav3392. <https://doi.org/10.1126/science.aav3392>.
- [23] Kopasov, A.A.; Mel'nikov, A.S. Multiple topological transitions driven by the interplay of normal scattering and Andreev scattering. *Phys. Rev. B* **2020**, *101*, 054515. <https://doi.org/10.1103/PhysRevB.101.054515>.

- [24] Denisov, A.O.; Bubis, A.V.; Piatrusha, S.U.; Titova, N.A.; Nasibulin, A.G.; Becker, J.; Treu, J.; Ruhstorfer, D.; Koblmüller, G.; Tikhonov, E.S.; et al. Charge-neutral nonlocal response in superconductor-InAs nanowire hybrid devices. *Semicond. Sci. Technol.* **2021**, *36*, 09LT04. <https://doi.org/10.1088/1361-6641/ac187b>.
- [25] Keizer, R.S.; Flokstra, M.G.; Aarts, J.; Klapwijk, T.M. Critical Voltage of a Mesoscopic Superconductor. *Phys. Rev. Lett.* **2006**, *96*, 147002. <https://doi.org/10.1103/PhysRevLett.96.147002>.
- [26] Hübler, F.; Lemyre, J.C.; Beckmann, D.; Löhneysen, H.V. Charge imbalance in superconductors in the low-temperature limit. *Phys. Rev. B* **2010**, *81*, 184524. <https://doi.org/10.1103/PhysRevB.81.184524>.
- [27] Vercruyssen, N.; Verhagen, T.G.A.; Flokstra, M.G.; Pekola, J.P.; Klapwijk, T.M. Evanescent states and nonequilibrium in driven superconducting nanowires. *Phys. Rev. B* **2012**, *85*, 224503. <https://doi.org/10.1103/PhysRevB.85.224503>.
- [28] Golikova, T.E.; Wolf, M.J.; Beckmann, D.; Batov, I.E.; Bobkova, I.V.; Bobkov, A.M.; Ryazanov, V.V. Nonlocal supercurrent in mesoscopic multiterminal SNS Josephson junction in the low-temperature limit. *Phys. Rev. B* **2014**, *89*, 104507. <https://doi.org/10.1103/PhysRevB.89.104507>.
- [29] Bergeret, F.S.; Silaev, M.; Virtanen, P.; Heikkilä, T.T. Colloquium: Nonequilibrium effects in superconductors with a spin-splitting field. *Rev. Mod. Phys.* **2018**, *90*, 041001. <https://doi.org/10.1103/RevModPhys.90.041001>.
- [30] Kuzmanović, M.; Wu, B.Y.; Weideneder, M.; Quay, C.H.L.; Aprili, M. Evidence for spin-dependent energy transport in a superconductor. *Nat. Commun.* **2020**, *11*, 4336.
- [31] Bubis, A.V.; Shpagina, E.V.; Nasibulin, A.G.; Khrapai, V.S. Thermal conductance and nonequilibrium superconductivity in a diffusive NSN wire probed by shot noise. *Phys. Rev. B* **2021**, *104*, 125409. <https://doi.org/10.1103/physrevb.104.125409>.
- [32] Nagaev, K.E.; Büttiker, M. Semiclassical theory of shot noise in disordered superconductor–normal-metal contacts. *Phys. Rev. B* **2001**, *63*, 081301. <https://doi.org/10.1103/PhysRevB.63.081301>.
- [33] Kozhevnikov, A.A.; Schoelkopf, R.J.; Prober, D.E. Observation of Photon-Assisted Noise in a Diffusive Normal Metal–Superconductor Junction. *Phys. Rev. Lett.* **2000**, *84*, 3398–3401. <https://doi.org/10.1103/PhysRevLett.84.3398>.

- [34] Jehl, X.; Sanquer, M.; Calemczuk, R.; Mailly, D. Detection of doubled shot noise in short normal-metal/superconductor junctions. *Nature* **2000**, *405*, 50–53. <https://doi.org/10.1038/35011012>.
- [35] Courtois, H.; Charlat, P.; Gandit, P.; Mailly, D.; Pannetier, B. The Spectral Conductance of a Proximity Superconductor and the Reentrance Effect. *J. Low Temp. Phys.* **1999**, *116*, 187–213. <https://doi.org/10.1023/a:1021885617107>.
- [36] Eom, J.; Chien, C.J.; Chandrasekhar, V. Phase Dependent Thermopower in Andreev Interferometers. *Phys. Rev. Lett.* **1998**, *81*, 437–440. <https://doi.org/10.1103/physrevlett.81.437>.
- [37] Rosdahl, T.O.; Vuik, A.; Kjaergaard, M.; Akhmerov, A.R. Andreev rectifier: A nonlocal conductance signature of topological phase transitions. *Phys. Rev. B* **2018**, *97*, 045421. <https://doi.org/10.1103/PhysRevB.97.045421>.
- [38] Anantram, M.P.; Datta, S. Current fluctuations in mesoscopic systems with Andreev scattering. *Phys. Rev. B* **1996**, *53*, 16390–16402. <https://doi.org/10.1103/PhysRevB.53.16390>.
- [39] Steinbach, A.H.; Martinis, J.M.; Devoret, M.H. Observation of Hot-Electron Shot Noise in a Metallic Resistor. *Phys. Rev. Lett.* **1996**, *76*, 3806–3809. <https://doi.org/10.1103/PhysRevLett.76.3806>.
- [40] Henny, M.; Oberholzer, S.; Strunk, C.; Schönenberger, C. $1/3$ -shot-noise suppression in diffusive nanowires. *Phys. Rev. B* **1999**, *59*, 2871–2880. <https://doi.org/10.1103/PhysRevB.59.2871>.
- [41] Tikhonov, E.S.; Shovkun, D.V.; Ercolani, D.; Rossella, F.; Rocci, M.; Sorba, L.; Roddaro, S.; Khrapai, V.S. Local noise in a diffusive conductor. *Sci. Rep.* **2016**, *6*, 30621.
- [42] Ronen, Y.; Cohen, Y.; Kang, J.H.; Haim, A.; Rieder, M.T.; Heiblum, M.; Mahalu, D.; Shtrikman, H. Charge of a quasiparticle in a superconductor. *Proc. Natl. Acad. Sci. USA* **2016**, *113*, 1743–1748. <https://doi.org/10.1073/pnas.1515173113>.
- [43] Tikhonov, E.S.; Shovkun, D.V.; Snelder, M.; Stehno, M.P.; Huang, Y.; Golden, M.S.; Golubov, A.A.; Brinkman, A.; Khrapai, V.S. Andreev Reflection in an s -Type Superconductor Proximized 3D Topological Insulator. *Phys. Rev. Lett.* **2016**, *117*, 147001. <https://doi.org/10.1103/PhysRevLett.117.147001>.
- [44] Nagaev, K. On the shot noise in dirty metal contacts. *Phys. Lett. A* **1992**, *169*, 103–107. [https://doi.org/10.1016/0375-9601\(92\)90814-3](https://doi.org/10.1016/0375-9601(92)90814-3).
- [45] Das, A.; Ronen, Y.; Most, Y.; Oreg, Y.; Heiblum, M.; Shtrikman, H. Zero-bias peaks and split-

- ting in an Al–InAs nanowire topological superconductor as a signature of Majorana fermions. *Nat. Phys.* **2012**, *8*, 887–895. <https://doi.org/10.1038/nphys2479>.
- [46] Wu, P.M.; Gooth, J.; Zianni, X.; Svensson, S.F.; Glusckke, J.G.; Dick, K.A.; Thelander, C.; Nielsch, K.; Linke, H. Large Thermoelectric Power Factor Enhancement Observed in InAs Nanowires. *Nano Lett.* **2013**, *13*, 4080–4086. <https://doi.org/10.1021/nl401501j>.
- [47] Tikhonov, E.S.; Shovkun, D.V.; Ercolani, D.; Rossella, F.; Rocci, M.; Sorba, L.; Roddaro, S.; Khrapai, V.S. Noise thermometry applied to thermoelectric measurements in InAs nanowires. *Semicond. Sci. Technol.* **2016**, *31*, 104001. <https://doi.org/10.1088/0268-1242/31/10/104001>.
- [48] Hofstetter, L.; Csonka, S.; Baumgartner, A.; Fülöp, G.; d’Hollosy, S.; Nygård, J.; Schönenberger, C. Finite-Bias Cooper Pair Splitting. *Phys. Rev. Lett.* **2011**, *107*, 136801. <https://doi.org/10.1103/PhysRevLett.107.136801>.
- [49] Ménard, G.C.; Anselmetti, G.L.R.; Martinez, E.A.; Puglia, D.; Malinowski, F.K.; Lee, J.S.; Choi, S.; Pendharkar, M.; Palmstrøm, C.J.; Flensberg, K.; et al. Conductance-Matrix Symmetries of a Three-Terminal Hybrid Device. *Phys. Rev. Lett.* **2020**, *124*, 036802. <https://doi.org/10.1103/PhysRevLett.124.036802>.
- [50] Puglia, D.; Martinez, E.A.; Ménard, G.C.; Pöschl, A.; Gronin, S.; Gardner, G.C.; Kallagher, R.; Manfra, M.J.; Marcus, C.M.; Higginbotham, A.P.; et al. Closing of the induced gap in a hybrid superconductor-semiconductor nanowire. *Phys. Rev. B* **2021**, *103*, 235201. <https://doi.org/10.1103/PhysRevB.103.235201>.
- [51] Tikhonov, E.S.; Denisov, A.O.; Piatrusha, S.U.; Khrapach, I.N.; Pekola, J.P.; Karimi, B.; Jabdaraghi, R.N.; Khrapai, V.S. Spatial and energy resolution of electronic states by shot noise. *Phys. Rev. B* **2020**, *102*, 085417. <https://doi.org/10.1103/PhysRevB.102.085417>.
- [52] Linder, J.; Robinson, J.W.A. Superconducting spintronics. *Nat. Phys.* **2015**, *11*, 307–315. <https://doi.org/10.1038/nphys3242>.
- [53] Schaibley, J.R.; Yu, H.; Clark, G.; Rivera, P.; Ross, J.S.; Seyler, K.L.; Yao, W.; Xu, X. Valleytronics in 2D materials. *Nat. Rev. Mater.* **2016**, *1*, 16055. <https://doi.org/10.1038/natrevmats.2016.55>.
- [54] Meair, J.; Stano, P.; Jacquod, P. Measuring spin accumulations with current noise. *Phys. Rev. B* **2011**, *84*, 073302. <https://doi.org/10.1103/PhysRevB.84.073302>.
- [55] Arakawa, T.; Shiogai, J.; Ciorga, M.; Utz, M.; Schuh, D.; Kohda, M.; Nitta, J.; Bougeard, D.; Weiss, D.; Ono, T.; et al. Shot Noise Induced by Nonequilibrium Spin Accumulation. *Phys.*

- Rev. Lett.* **2015**, *114*, 016601. <https://doi.org/10.1103/PhysRevLett.114.016601>.
- [56] Khrapai, V.S.; Nagaev, K.E. Current noise generated by spin imbalance in presence of spin relaxation. *JETP Lett.* **2017**, *105*, 18–20. <https://doi.org/10.1134/s0021364017010015>.
- [57] Ludwig, T.; Burmistrov, I.S.; Gefen, Y.; Shnirman, A. Current noise geometrically generated by a driven magnet. *Phys. Rev. Res.* **2020**, *2*, 023221. <https://doi.org/10.1103/PhysRevResearch.2.023221>.
- [58] Read, N.; Green, D. Paired states of fermions in two dimensions with breaking of parity and time-reversal symmetries and the fractional quantum Hall effect. *Phys. Rev. B* **2000**, *61*, 10267–10297. <https://doi.org/10.1103/PhysRevB.61.10267>.
- [59] Wang, Z.; Qi, X.L.; Zhang, S.C. Topological field theory and thermal responses of interacting topological superconductors. *Phys. Rev. B* **2011**, *84*, 014527. <https://doi.org/10.1103/PhysRevB.84.014527>.
- [60] Akhmerov, A.R.; Dahlhaus, J.P.; Hassler, F.; Wimmer, M.; Beenakker, C.W.J. Quantized Conductance at the Majorana Phase Transition in a Disordered Superconducting Wire. *Phys. Rev. Lett.* **2011**, *106*, 057001. <https://doi.org/10.1103/PhysRevLett.106.057001>.
- [61] Bagrets, D.; Altland, A.; Kamenev, A. Sinai Diffusion at Quasi-1D Topological Phase Transitions. *Phys. Rev. Lett.* **2016**, *117*, 196801. <https://doi.org/10.1103/PhysRevLett.117.196801>.
- [62] Kasahara, Y.; Ohnishi, T.; Mizukami, Y.; Tanaka, O.; Ma, S.; Sugii, K.; Kurita, N.; Tanaka, H.; Nasu, J.; Motome, Y.; et al. Majorana quantization and half-integer thermal quantum Hall effect in a Kitaev spin liquid. *Nature* **2018**, *559*, 227–231. <https://doi.org/10.1038/s41586-018-0274-0>.
- [63] Kejriwal, A.; Muralidharan, B. Nonlocal conductance and the detection of Majorana zero modes: Insights from von Neumann entropy. *Phys. Rev. B* **2022**, *105*, L161403. <https://doi.org/10.1103/PhysRevB.105.L161403>
- [64] Blanter, Y.; Büttiker, M. Shot noise in mesoscopic conductors *Physics Reports* **2000**, *336*, 1. [https://doi.org/10.1016/S0370-1573\(99\)00123-4](https://doi.org/10.1016/S0370-1573(99)00123-4)
- [65] Bubis, A.V.; Denisov, A.O.; Piatrusha, S.U.; Batov, I.E.; Khrapai, V.S.; Becker, J.; Treu, J.; Ruhstorfer, D.; Koblmüller, G.; Proximity effect and interface transparency in al/InAs-nanowire/al diffusive junctions *Semiconductor Science and Technology* **2017**, *32*, 094007. <https://doi.org/10.1088/1361-6641/aa7eef>
- [66] Hertenberger, S.; Rudolph, D.; Bichler, M.; Finley, J.J.; Abstreiter, G.; Koblmüller, G.;

- Growth kinetics in position-controlled and catalyst-free InAs nanowire arrays on Si(111) grown by selective area molecular beam epitaxy *Journal of Applied Physics* **2010**, *108*, 114316.
<https://doi.org/10.1063/1.3525610>
- [67] Becker, J.; Morkötter, S.; Treu, J.; Sonner, M.; Speckbacher, M.; Döblinger, M.; Abstreiter, G.; Finley, J.J.; Koblmüller, G. Carrier trapping and activation at short-period wurtzite/zinc-blende stacking sequences in polytypic inas nanowires *Phys. Rev. B* **2018**, *97*, 115306.
<https://doi.org/10.1103/PhysRevB.97.115306>

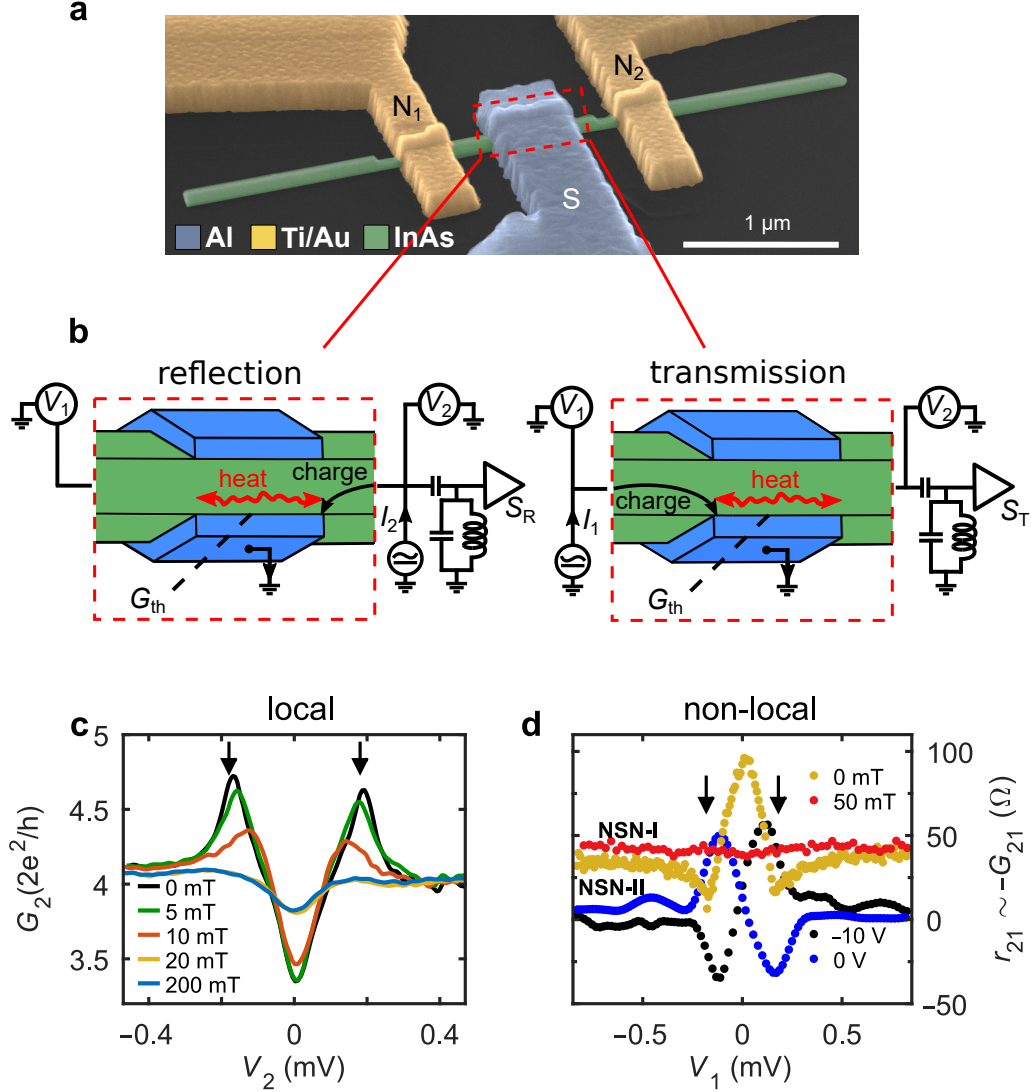


FIG. 1. Outline and charge transport data. (a) Scanning electron microscope image of the typical device (false color). InAs NW is equipped with two N terminals (Ti/Au) on the sides and one S-terminal (Al) in the middle. (b) Separation of charge and heat currents at the InAs/Al interface and two noise measurement configurations. The three-terminal device layout allows studying thermal conductance G_{th} of the proximitized NW region by measuring shot noise in the transmission configuration. Note that in the present experiment, only terminal N2 is connected to the low temperature amplifier, so that switching between the reflection noise S_R and transmission noise S_T is achieved by interchanging the biased and floating N-terminals, see the Supplemental Materials for the wiring scheme. (c) Local differential conductance of NS junction in device NSN-II measured at $T = 50$ mK in different magnetic fields. (d) Non-local differential resistance $r_{21} \equiv dV_2/dI_1$ for two devices plotted at different B and V_g .

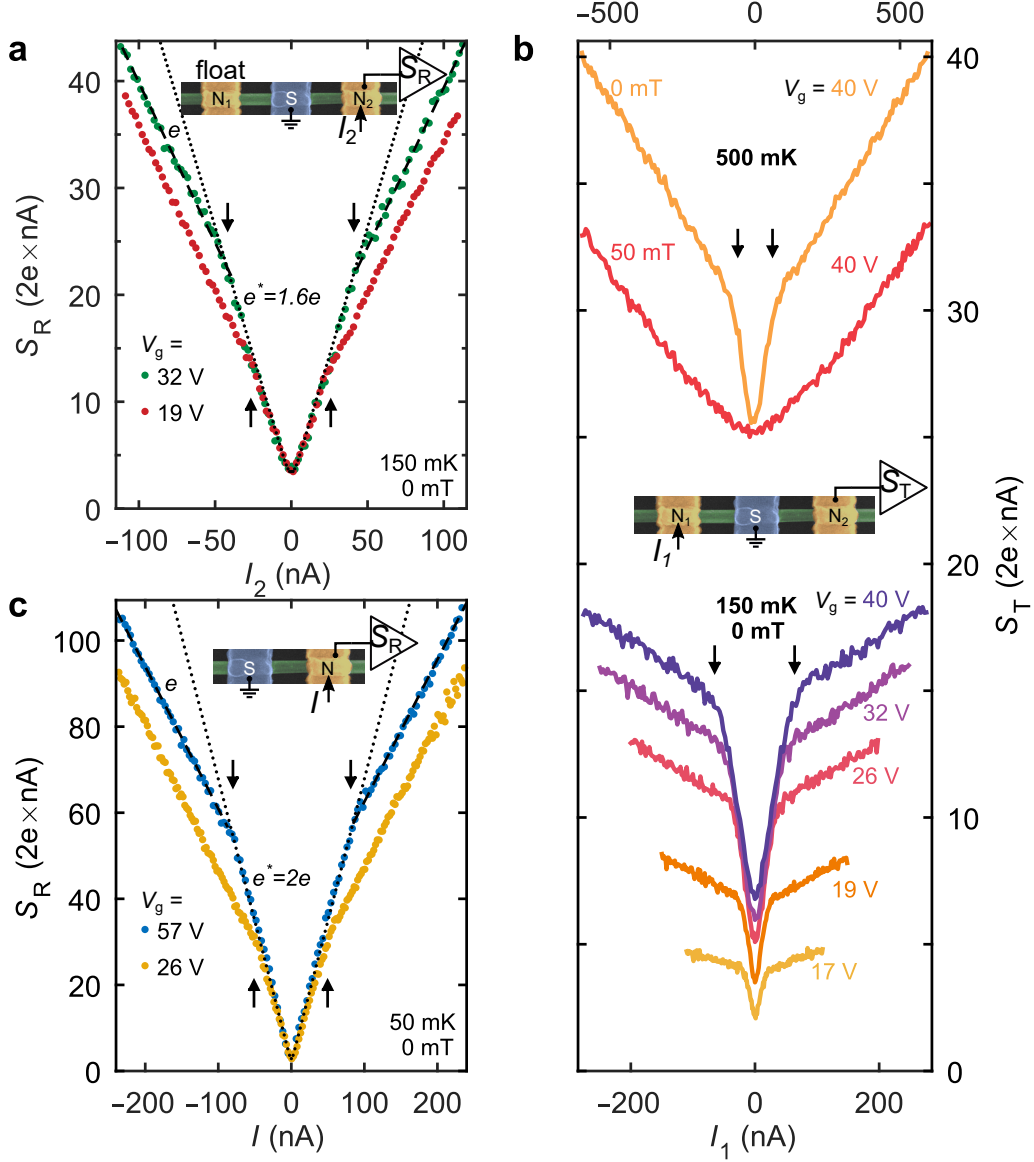


FIG. 2. Reflected and transmitted shot noise. (a) Reflection noise configuration in device NSN-I. Noise spectral density of the biased NS junction as a function of current at two values of V_g . Dotted line is the fit with $F = 0.30$ and charge $e^* = 1.6e$; dashed line slope corresponds to $F = 0.30$ and charge equal to e . Green symbols are shifted vertically by $9 \times 10^{-28} \text{ A}^2/\text{Hz}$ to coincide with red ones at zero bias. (b) Transmission noise configuration in device NSN-I. Noise spectral density of the floating NS junction as a function of current at different B , T and V_g (see legend). (c) Reflected shot noise in the reference two-terminal NS device as a function of current at two values of V_g . Dotted line is the fit with $F = 0.33$, $e^* = 2e$; dashed line slope corresponds to $F = 0.33$ and charge equal to e .

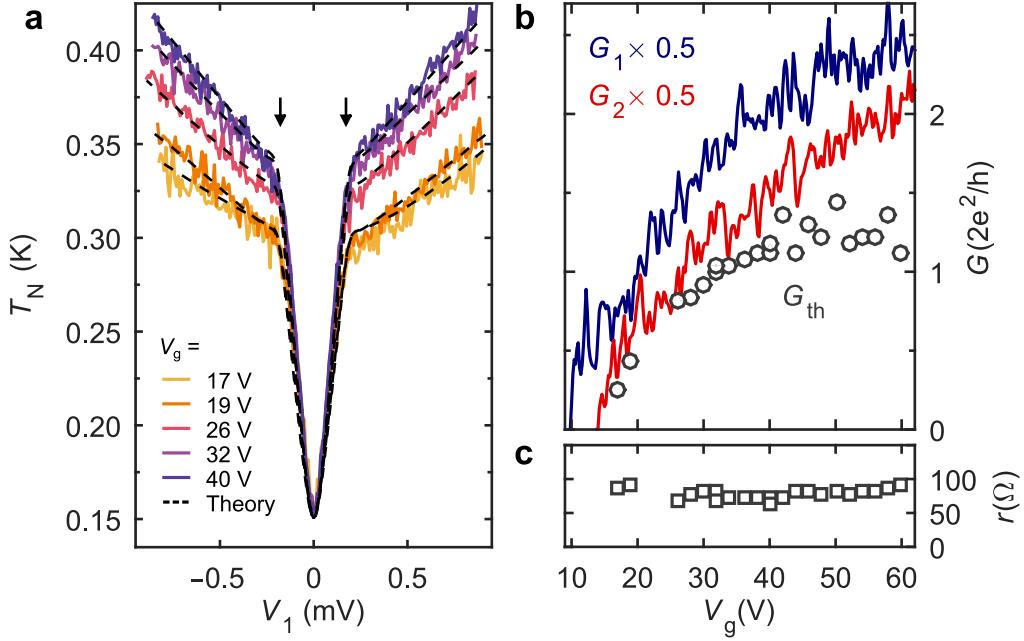


FIG. 3. Thermal conductance in the device NSN-I. (a) Noise temperature T_N measured in the transmission configuration as a function of bias (solid lines, same data as in the lower part of Figure 2b) along with the model fits (dashed lines). (b,c) (symbols) Sub-gap thermal conductance G_{th} and interface resistance parameter r plotted as a function of V_g . (lines) Linear response conductances of the left/right ($G_{1/2}$) NS junctions.

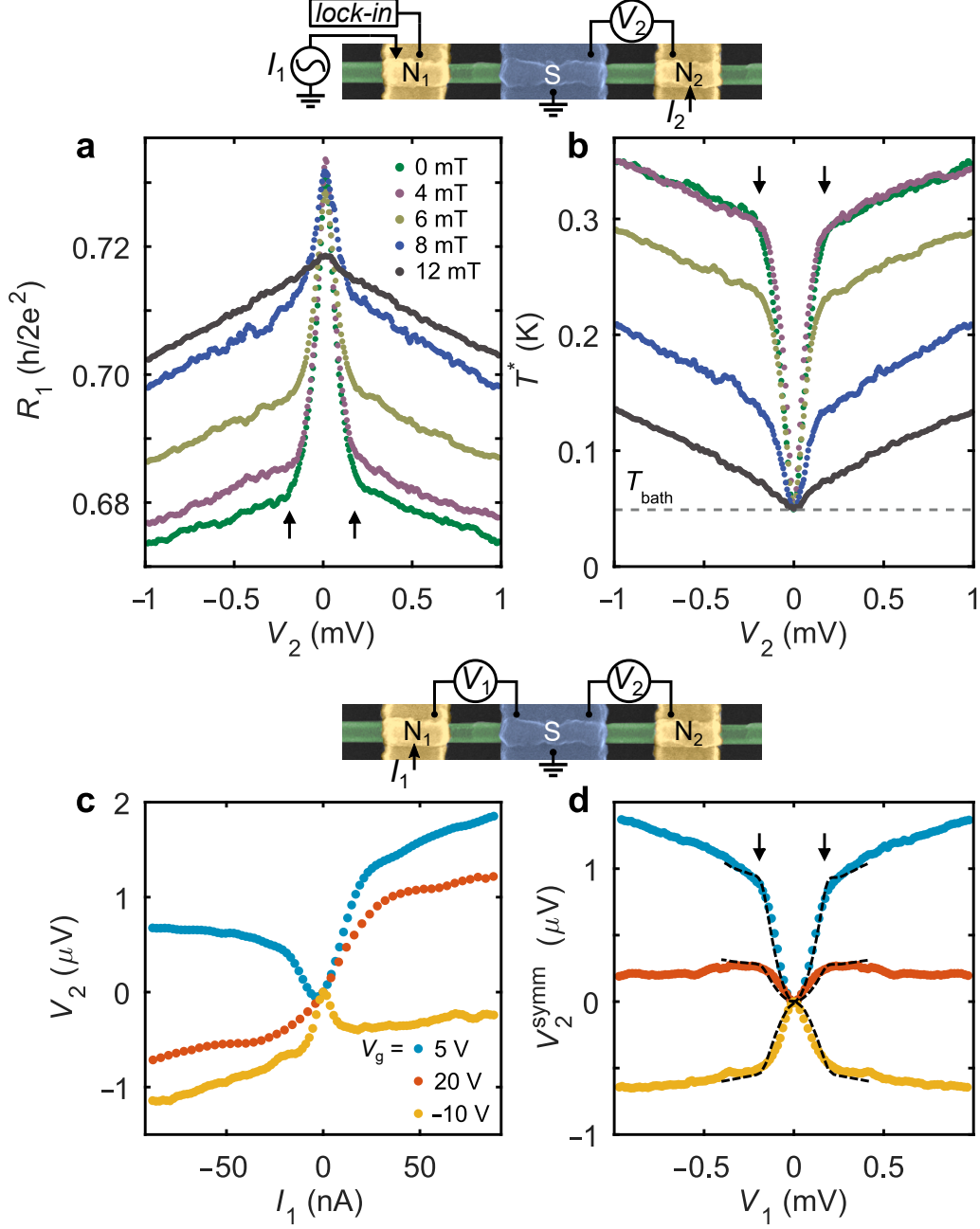


FIG. 4. Resistive thermometry and non-local I - V s in device NSN-II. (a) Linear response resistance of the floating NS junction as a function of bias in the neighboring junction. (b) The same data converted to the effective temperature T^* . (c) The non-local I - V characteristics measured at three representative V_g values. (d) Symmetric component of the non-local I - V s. The dashed lines are the calculated thermoelectric voltage values for different energy-independent Seebeck coefficients of $S/T = 3.0$ μ V/K², 0.9 μ V/K² and -3.6 μ V/K² (from top to bottom). Upper sketch: setup for resistive thermometry. Lower sketch: setup for non-local I - V s.

Heat-mode excitation in a proximity superconductor.

Supplemental Materials

A.O. Denisov,^{1,2} A.V. Bubis,^{3,1} S.U. Piatrusha,¹ N.A. Titova,⁴ A.G. Nasibulin,³
J. Becker,⁵ J. Treu,⁵ D. Ruhstorfer,⁵ G. Koblmüller,⁵ E.S. Tikhonov,¹ and V.S. Khrapai^{1,6}

¹*Osipyan Institute of Solid State Physics,
Russian Academy of Sciences, 142432 Chernogolovka, Russia*

²*Department of Physics, Princeton University,
Princeton, New Jersey 08544, USA*

³*Skolkovo Institute of Science and Technology,
Nobel street 3, 121205 Moscow, Russian Federation*

⁴*Moscow Pedagogical State University,
29 Malaya Pirogovskaya St, 119435 Moscow, Russia*

⁵*Walter Schottky Institut, Physik Department,
and Center for Nanotechnology and Nanomaterials,
Technische Universität München, Am Coulombwall 4, Garching 85748, Germany*

⁶*National Research University Higher School of Economics,
20 Myasnitskaya Street, 101000 Moscow, Russia*

Abstract

This file contains supplementary information for the main text, including the following figures:

Figure S1: Sketch of the experimental setup

Figure S2: Calibration via equilibrium noise

Figure S3: Shot-noise analysis

Figure S4: Additional data in device NSN-I: local conductance

Figure S5: Additional data in device NSN-II: local conductance

Figure S6: Additional data in device NSN-I: non-local conductance

Figure S7: Additional data in device NSN-II: non-local conductance

Figure S8: Effective resistance model for NW/S interface

Figure S9: T-dependence in the linear response regime and calibration of the resistive thermometry

Figure S10: T-dependence beyond the linear response regime

Figure S11: Analytical model: layout and EED

Figure S12: Analytical model: results

Figure S13: Comparison of the non-local noise thermometry and resistive thermometry

Figure S14: Superconducting critical temperature of the Al-film

Noise and charge transport measurements

DC and low frequency AC transport measurements are carried out using symmetric current bias scheme with divider shown in Fig. S1. We use quasi-4-terminal setup thus excluding wiring and filtering contribution into measured voltage signal. We use SR-7265 lock-in for resistive thermometry with typical modulation current of 2 nA, $f = 19.3$ Hz, time constant = 2s, AC gain 30 dB and filter slope of 24 dB/oct.

The noise spectral density was measured using the home-made low-temperature amplifier (LTamp) with a voltage gain of about 10dB and the input current noise of $\sim 2-6 \times 10^{-27}$ A²/Hz. The voltage fluctuations on a 25 k Ω load resistance were measured near the central frequency 14.2 MHz (± 0.6 MHz for -3 dB point) of a resonant circuit at the input of the LTamp. The output of the LTamp was fed into the low noise 75 dB gain room temperature amplification stage followed by a hand-made analogue band-pass filter and a power detector. The setup was calibrated using HEMT ATF-35143 as adjustable load

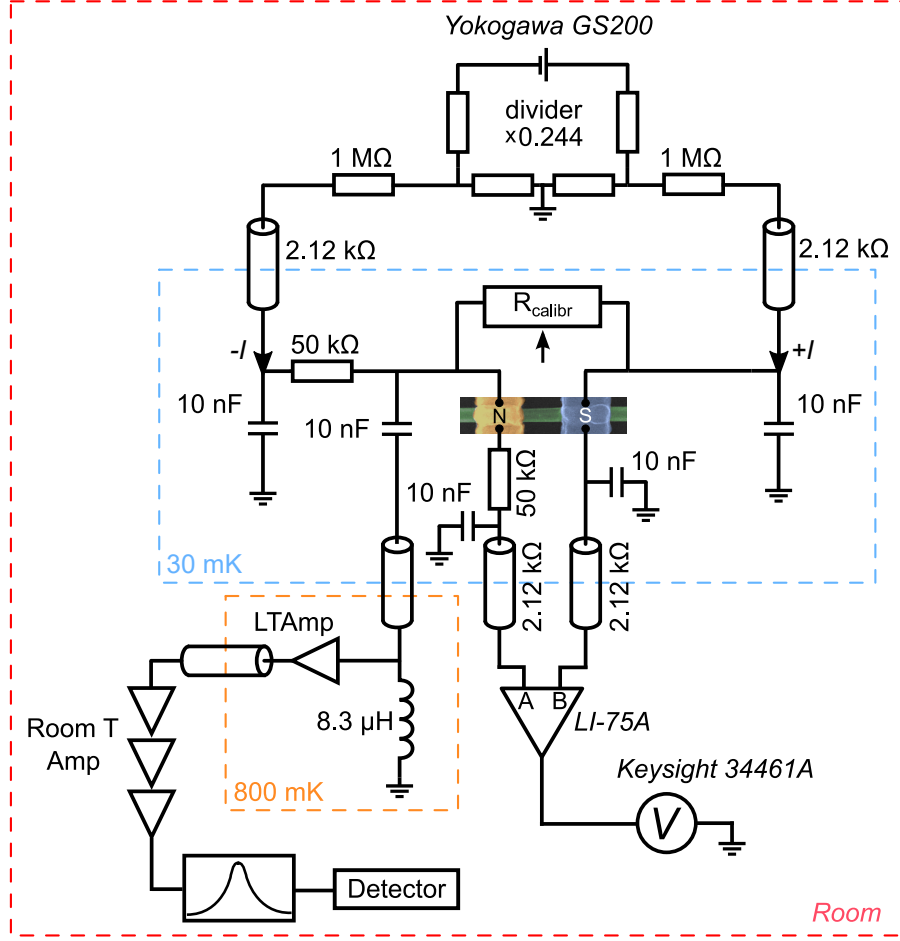


FIG. S1. Sketch of the experimental setup.

$R_{\text{calib}} = 50 \, \Omega \rightarrow > 100 \, \text{M}\Omega$ for the equilibrium Johnson-Nyquist noise thermometry. Except for the periods of calibration, the transistor was always kept pinched off. Unless otherwise stated, the measurements were performed in a cryogenic free Bluefors dilution refrigerator BF-LD250 at a bath temperature of 30 mK.

Johnson-Nyquist noise thermometry

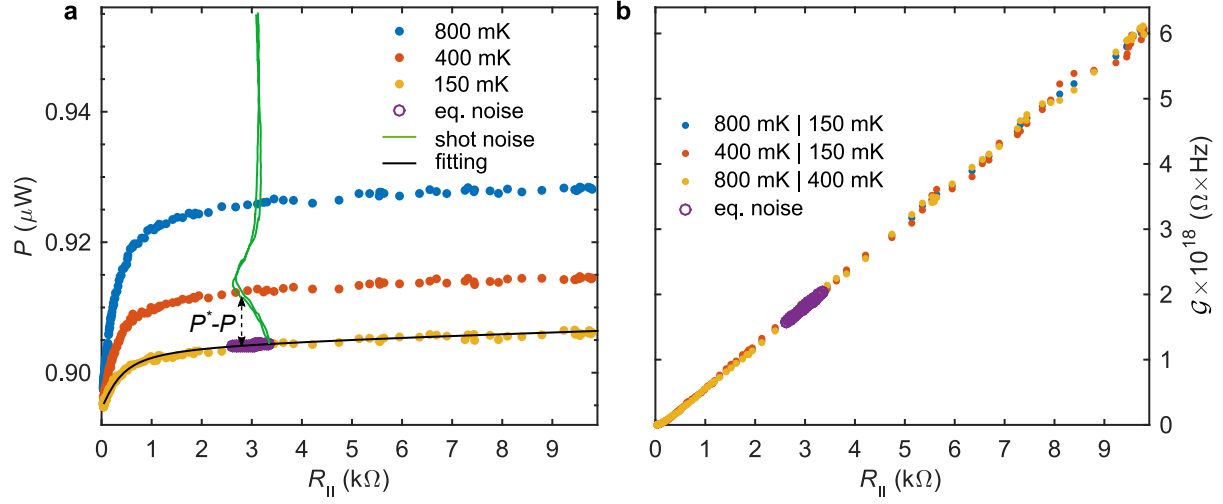


FIG. S2. **Calibration via equilibrium noise.** (a) Power released on the detector as a function of total load resistance $R_{||}$ measured at different bath temperatures (see electron temperature in the legend). Green solid line shows typical reflected shot-noise signal at applying bias current through the device (NSN - I, $V_g = 40$ V). Black solid line is fit using Nyquist relation. Purple circles shows bias-dependent gain and equilibrium noise. (b) Total gain of the setup. Three sets of points correspond to three different combinations of $T_1|T_2$ (see text below).

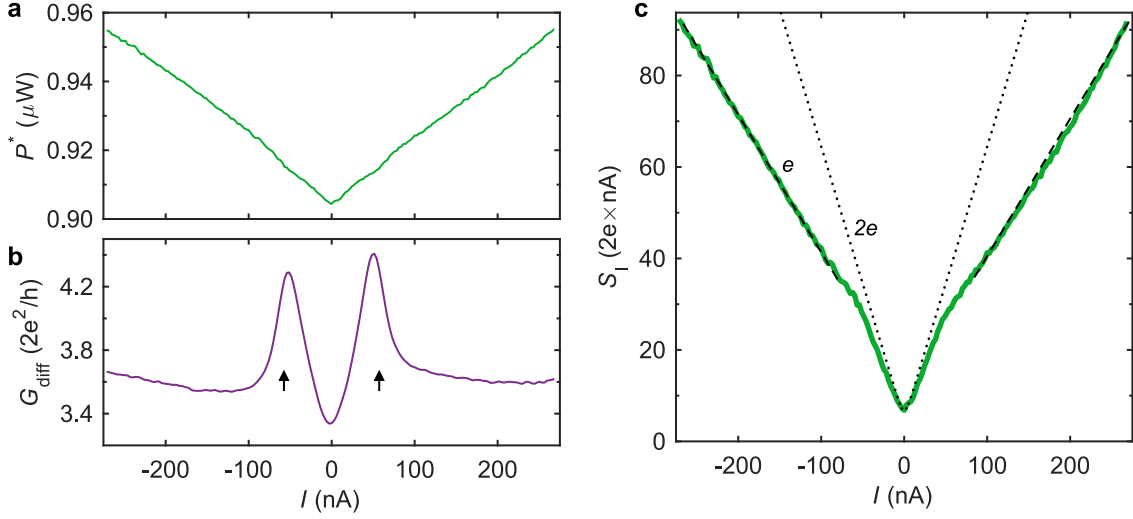


FIG. S3. **Shot-noise analysis.** (a) Power dissipated in the detector is plotted as a function of current through the sample. (b) Differential conductance of the NS junction. Arrows mark superconducting gap $\pm\Delta$. (c) Extracted current noise spectral density. Dashed line corresponds to Fano-factor $F = S_I/2eI = 0.30$ and $e^* = e$, dotted line is for doubled charge - $F = 0.30$ and $e^* = 2e$.

We calibrate our setup using equilibrium noise thermometry. At zero current through the device, we are able to change a value of $R_{||} = (G_{\text{diff}} + R_{25\text{k}\Omega}^{-1} + R_{\text{calibr}}^{-1})^{-1}$ drastically, where G_{diff} is a differential resistance (zero bias) of the sample shown in Fig. S3b. Power released on the detector after all amplification stages :

$$P(R_{||}) = \left(\frac{4k_{\text{B}}T}{R_{||}} + S_{\text{I}}^{\text{Amp}} \right) \int \frac{G \times Tr^{\text{filter}}(f)}{R_{||}^{-2} + |Z_{\text{LC}}|^{-2}} df + P_0 = \mathcal{G}(R_{||}) \left(\frac{4k_{\text{B}}T}{R_{||}} + S_{\text{I}}^{\text{Amp}} \right) + P_0 \quad (\text{S1})$$

where G is an unknown total gain, Z_{LC} - complex impedance of the LC contour, $Tr^{\text{filter}}(f)$ - transmission characteristic of the band-pass filter, $S_{\text{I}}^{\text{Amp}}$ and P_0 - parasitic current noise and background of the low-temperature amplifier. After an integration over frequency, we can use generalized value for gain $\mathcal{G}(R_{||})$ which can be extracted by measuring $P(R_{||})$ at different bath temperatures:

$$\mathcal{G}(R_{||}) = \frac{P(R_{||}, T_1) - P(R_{||}, T_2)}{T_1 - T_2} \frac{R_{||}}{4k_{\text{B}}} \quad (\text{S2})$$

When we apply current through the sample, the crossover from thermal to non-equilibrium

shot noise (see solid green curve in Fig. S2a and Fig. S3a) appears. Depending on the bias current, $R_{||}(I)$ is changing thus making $\mathcal{G}(R_{||})$ bias-dependent (see purple symbols in Fig. S2a, b). Desired current noise of the sample S_I contributes to the total power as follows (transistor is pinched off $R_{\text{calib}} > 100 \text{ M}\Omega$) :

$$P^*(R_{||}) = \mathcal{G}(R_{||}) \left(\frac{4k_B T}{R_{25\text{k}\Omega}} + S_I + S_I^{\text{Amp}} \right) + P_0, \quad S_I = \frac{P^*(R_{||}) - P(R_{||})}{\mathcal{G}(R_{||})} + 4k_B T G_{\text{diff}} \quad (\text{S3})$$

Finalized current spectral density curve is shown in Fig. S3c.

Local charge transport

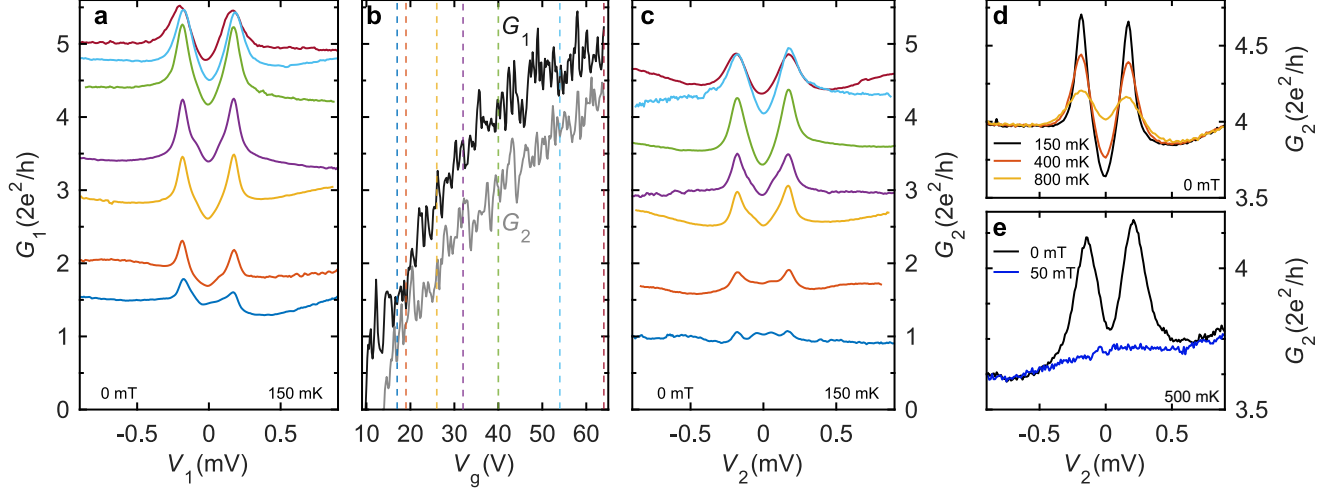


FIG. S4. **Additional data in device NSN-I: local conductance.** (a) and (c) Local spectral conductance of the left and right NS junctions correspondingly, measured at different back-gate voltages $V_g = 17, 19, 26, 32, 40, 54, 64$ V from bottom to top. (b) Linear-response conductance is plotted as function of V_g . Dashed lines of corresponding colors point certain values of back-gate voltages from (a) and (c). (d) and (e) Temperature and magnetic field dependence of the spectral conductance measured at constant $V_g = 41$ and 50 V correspondingly.

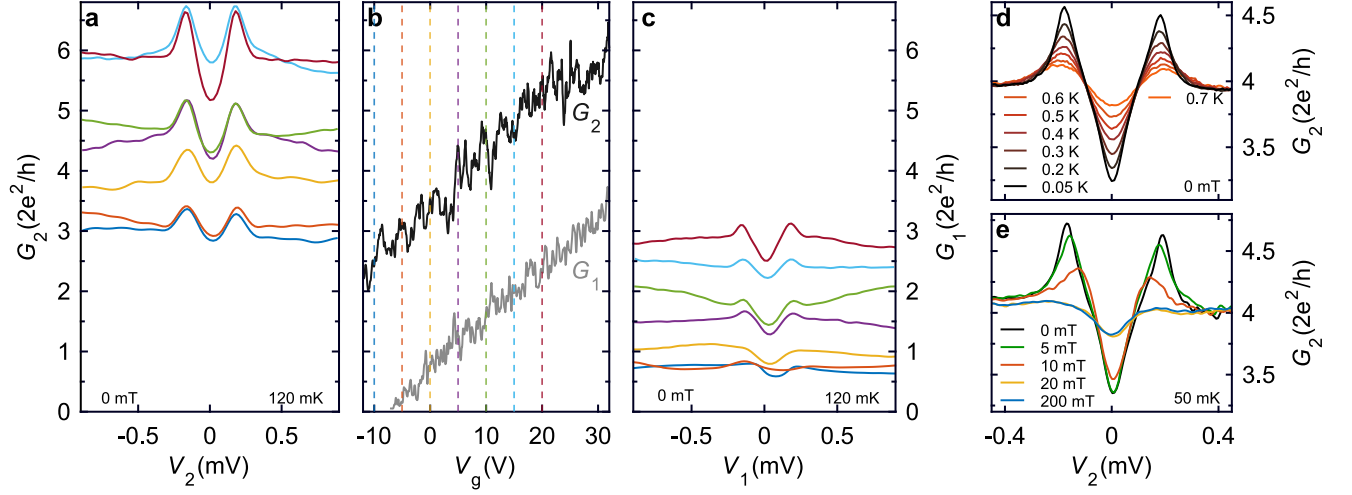


FIG. S5. **Additional data in device NSN-II: local conductance.** (a) and (c) Local spectral conductance of the left and right NS junctions correspondingly, measured at different back-gate voltages $V_g = -10, -5, 0, 5, 10, 15, 20$ V from bottom to top. (b) Linear-response conductance is plotted as function of V_g . Dashed lines of corresponding colors point certain values of back-gate voltages from (a) and (c). (d) and (e) Temperature and magnetic field dependence of the spectral conductance measured at constant $V_g = 0$ V.

Non-local charge transport

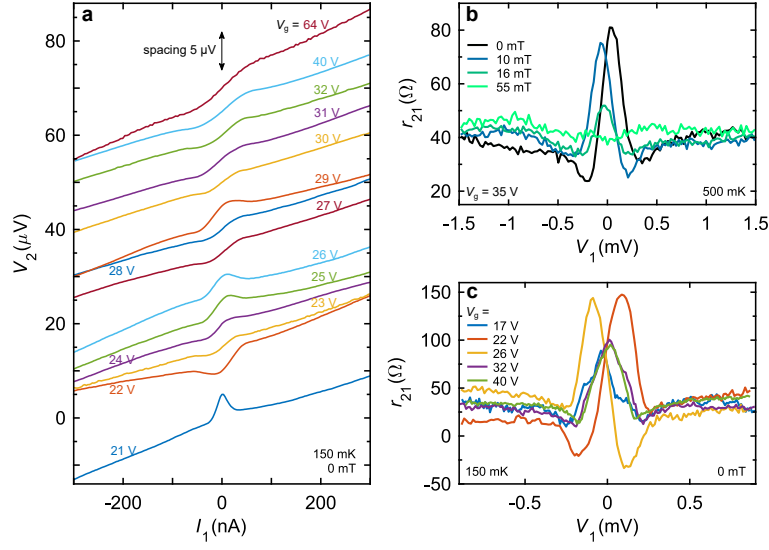


FIG. S6. **Additional data in device NSN-I: non-local conductance.** (a) Non-local I/V characteristics measured at different back-gate voltages. For convenience, curves are shifted vertically with spacing of 5 μV . (b) and (c) Differential non-local resistance $r_{21} = dV_2/dI_1$, $I_2 = 0$ at different magnetic fields and back-gate voltages correspondingly.

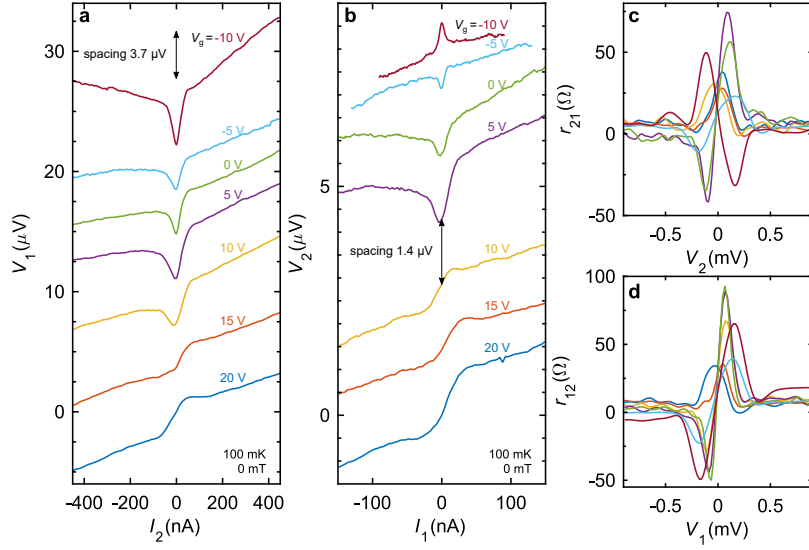


FIG. S7. **Additional data in device NSN-II: non-local conductance.** (a) and (b) Non-local I/V characteristics of both NS junctions measured at different back-gate voltages. For convenience, curves are shifted vertically with spacing of $3.7 \mu\text{V}$ and $1.4 \mu\text{V}$ correspondingly. (c) and (d) Differential non-local resistance $r_{21} = dV_2/dI_1$, $I_2 = 0$ and $r_{12} = dV_1/dI_2$, $I_1 = 0$ at different back-gate voltages. Colors match those from (a) and (b).

Current transfer length estimation

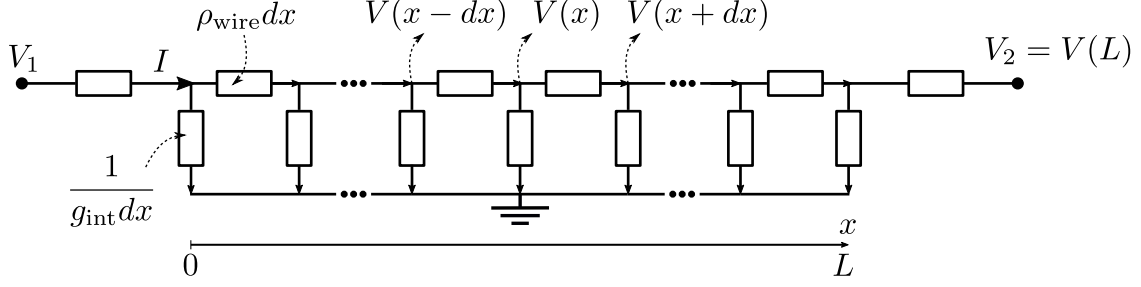


FIG. S8. **Effective resistance model for nanowire/superconductor interface.**

To estimate the characteristic length of charge overflow within grounded S terminal l_T we use circuit shown in fig. S8. Here ρ_{wire} and g_{int} are resistance of the nanowire (NW) and conductivity of interface per unit length respectively. In the continuous limit we can write current conservation for each point along NW/S interface:

$$\frac{V(x+dx) - V(x)}{\rho_{\text{wire}} dx} + \frac{V(x-dx) - V(x)}{\rho_{\text{wire}} dx} = \frac{V(x) dx}{1/g_{\text{int}}}$$

$$\frac{d^2 V(x)}{dx^2} = \frac{V(x)}{l_T^2}, \quad l_T = \frac{1}{\sqrt{\rho_{\text{wire}} g_{\text{int}}}}$$

Boundary conditions including one that normal terminal N2 is floating and no current flow into it.

$$\left. \frac{dV(x)}{dx} \right|_{x=0} = -\rho_{\text{wire}} I, \quad \left. \frac{dV(x)}{dx} \right|_{x=L} = 0$$

Solving elementary Neumann problem we can find non-local resistance r_{21} :

$$r_{21} = \frac{V(L)}{I} = \frac{l_T \rho_{\text{wire}}}{\sinh(\frac{L}{l_T})}$$

For two measured devices (NSN-I, NSN-II) we have $r_{21} \approx 40, 10 \Omega$ and $L \approx 200, 300 \text{ nm}$ respectively, thus $l_T \approx 75 \text{ nm}$.

Temperature dependence of differential conductance.

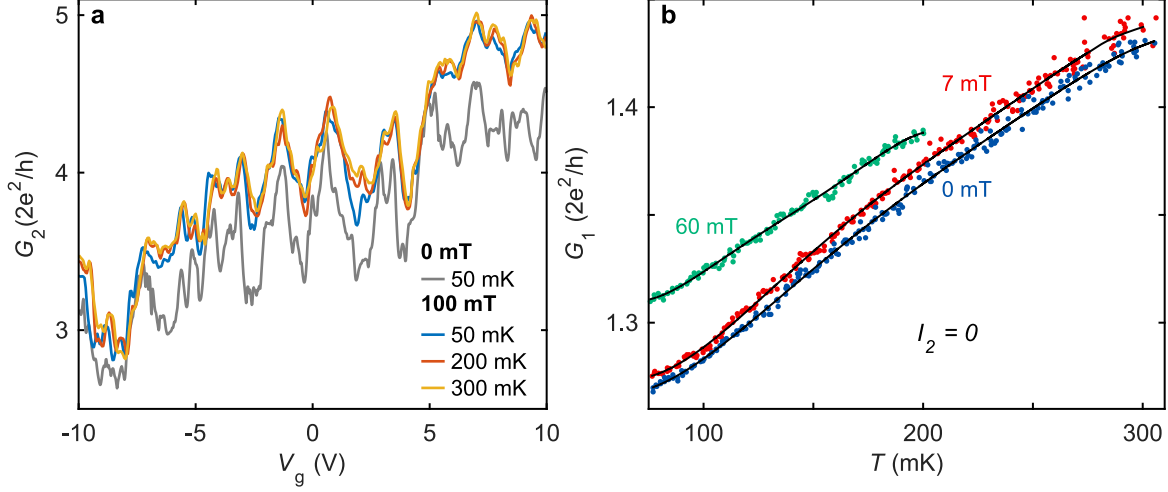


FIG. S9. T -dependence in the linear response regime and calibration of the resistive thermometry. (a) Linear-response conductance of a single NS junction (NSN - II device) measured at different bath temperatures. Overall increasing dependence with reproducible UCF persists up to the shift $\sim 10\%$ when large magnetic field ($100 \text{ mT} > B_c$) is applied. Such zero-bias deep is more evident from differential conductance data measured at $V_g = 0 \text{ V}$ and $I_2 = 0$ shown in (b). Solid lines are smooth polynomial fits we use for the resistive thermometry.

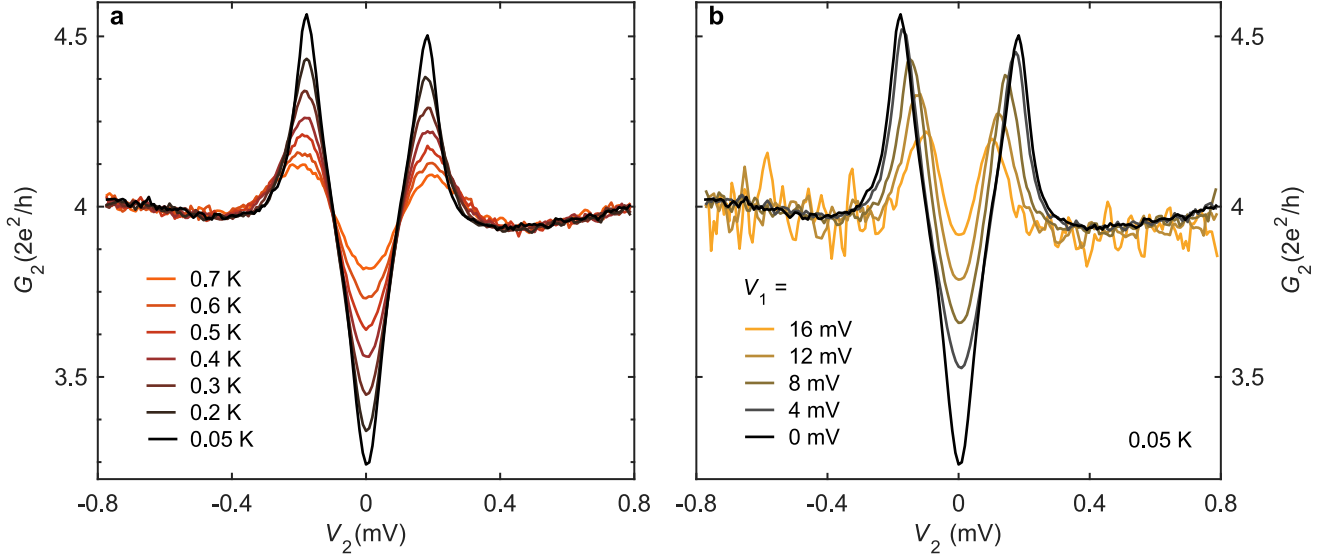


FIG. S10. **T -dependence beyond the linear response regime.** (a) Spectral conductance measured at constant $V_g = 0$ V (NSN - II device) and different bath temperatures. (b) Spectral conductance measured at constant $V_g = 0$ V, bath temperature but different "heating" voltages across the adjacent NS junction.

Analytical model

The sketch of analytical model we use to fit experimental data is shown in fig.3a. Since we operate in the non-linear $\varepsilon_T \sim k_B T \ll eV$ regime, where $\xi_T = \hbar D/L^2 \approx 15 \mu\text{V}$ is the Thouless energy, we can neglect the penetration of the condensate into NW and consider it just as a normal metal with a non-equilibrium electronic energy distribution (EED). Distribution functions near the N terminals $f_{1/2}(\varepsilon)$ are equilibrium Fermi-Dirac functions with local temperature and chemical potential of the corresponding terminal. EED near S should satisfy Andreev conditions for the energies below the gap:

$$f_{1/2}^*(\varepsilon) = \begin{cases} 1 - f_{1/2}^*(-\varepsilon) & |\varepsilon| < \Delta \\ (\exp(\varepsilon/k_B T) + 1)^{-1} & |\varepsilon| > \Delta \end{cases} \quad (\text{S4})$$

Following Nagaev and Buttiker [S1] we separately find electron distribution functions for energies below and above the gap and then sew them together. With EEDs near S terminal in hand, we are able to calculate current noise spectral density in both NS junction [S2] i.e.

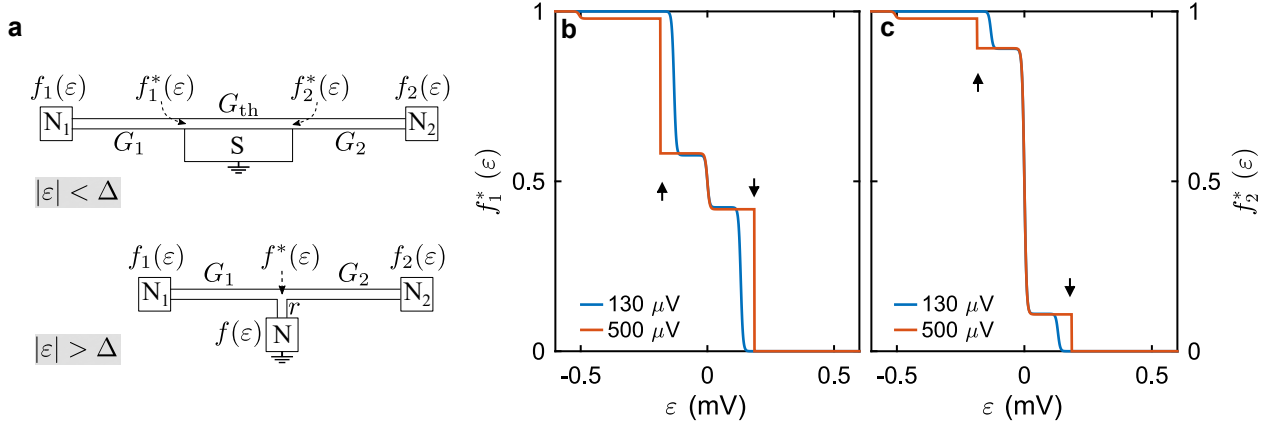


FIG. S11. **Analytical model: layout and EED.** (a) Schematics of the analytical model, separately for sub-gap and above-gap quasiparticle energies. (b) - (c) Calculated EEDs near two ends of the proximitized sections for $V_1 = 130 \mu V$ and $500 \mu V$ ($T = 50$ mK, $G_{th} = 1.17 \times 2e^2/h$, $r = 64 \Omega$). Arrows mark the superconducting gap of Al, $\Delta = 180 \mu V$.

reflected (R) and transmitted (T) shot noise:

$$S_{R/T} = \frac{2}{3} G_{1/2} \int \left[2f_{1/2}(\varepsilon)(1-f_{1/2}(\varepsilon)) + 2f_{1/2}^*(\varepsilon)(1-f_{1/2}^*(\varepsilon)) + f_{1/2}(\varepsilon)(1-f_{1/2}^*(\varepsilon)) + f_{1/2}^*(\varepsilon)(1-f_{1/2}(\varepsilon)) \right] d\varepsilon \quad (S5)$$

Sub-gap ($|\varepsilon| < \Delta$)

First we calculate for energies within the superconducting gap. Since noise temperature gradient is zero at N/S interface, then the correction to the noise temperature due to the finite r is of the second order and we can neglect it. In order to find the energy distributions $f_1^*(\varepsilon)$ and $f_2^*(\varepsilon)$ at the two ends of the proximitized wire section, one has to fulfill the continuity of the heat fluxes in these points at any given ε . In this way we get the following two equations:

$$G_2[f_2(\varepsilon) - f_2^*(\varepsilon)] - G_2[f_2(-\varepsilon) - f_2^*(-\varepsilon)] = G_{th}[f_2(\varepsilon) - f_1^*(\varepsilon)] - G_{th}[f_2(-\varepsilon) - f_1^*(-\varepsilon)] \quad (S6)$$

$$G_1[f_1(\varepsilon) - f_1^*(\varepsilon)] - G_1[f_1(-\varepsilon) - f_1^*(-\varepsilon)] = G_{th}[f_2(\varepsilon) - f_1^*(\varepsilon)] - G_{th}[f_2(-\varepsilon) - f_1^*(-\varepsilon)] \quad (S7)$$

where the terms with ε correspond to the particle heat flux and the terms with $-\varepsilon$ to the hole heat flux. The equations (S6) and (S7) are for the right and the left NS interface

respectively. For convinience lets introduce $F(\varepsilon) \equiv f(\varepsilon) - f(-\varepsilon)$, then:

$$F_1^*(\varepsilon) = \frac{G_1 G_2 F_1(\varepsilon) + G_{\text{th}} G_1 F_1(\varepsilon) + G_{\text{th}} G_2 F_2(\varepsilon)}{G_{\text{th}} G_1 + G_{\text{th}} G_2 + G_1 G_2}, \quad F_2^*(\varepsilon) = \frac{G_1 G_2 F_2(\varepsilon) + G_{\text{th}} G_2 F_2(\varepsilon) + G_{\text{th}} G_1 F_1(\varepsilon)}{G_{\text{th}} G_1 + G_{\text{th}} G_2 + G_1 G_2} \quad (\text{S8})$$

Since $f_i^*(\varepsilon) = 1 - f_i^*(-\varepsilon)$, we can easily find $f_i^* = (1 + F_i^*)/2$

Above-gap ($|\varepsilon| < \Delta$)

To calculate for energies above the superconducting gap, we need to take into account the fact that now there is a finite gradient of noise temperature near N/S interface. Then correction to T_N due to the finite r is of the first order and we can not neglect it. Fortunately, for energies above the gap, S terminal acts as regular normal lead, so we can assume $f^*(\varepsilon) = f_{1/2}^*(\varepsilon)$. In order to find $f^*(\varepsilon)$, one has to fulfill current conservation law for each energy:

$$G_2[f_2(\varepsilon) - f^*(\varepsilon)] + G_1[f_1(\varepsilon) - f^*(\varepsilon)] = r^{-1}[f^*(\varepsilon) - f_0(\varepsilon)] \quad (\text{S9})$$

where $f_0(\varepsilon)$ is a Fermi-Dirac distribution in the normal state of grounded Al terminal and r is the interface resistance.

$$f^*(\varepsilon) = \frac{G_1 f_1(\varepsilon) + G_2 f_2(\varepsilon) + 1/r f_0(\varepsilon)}{G_1 + G_2 + r^{-1}} \quad (\text{S10})$$

Reflected and Transmitted shot noise

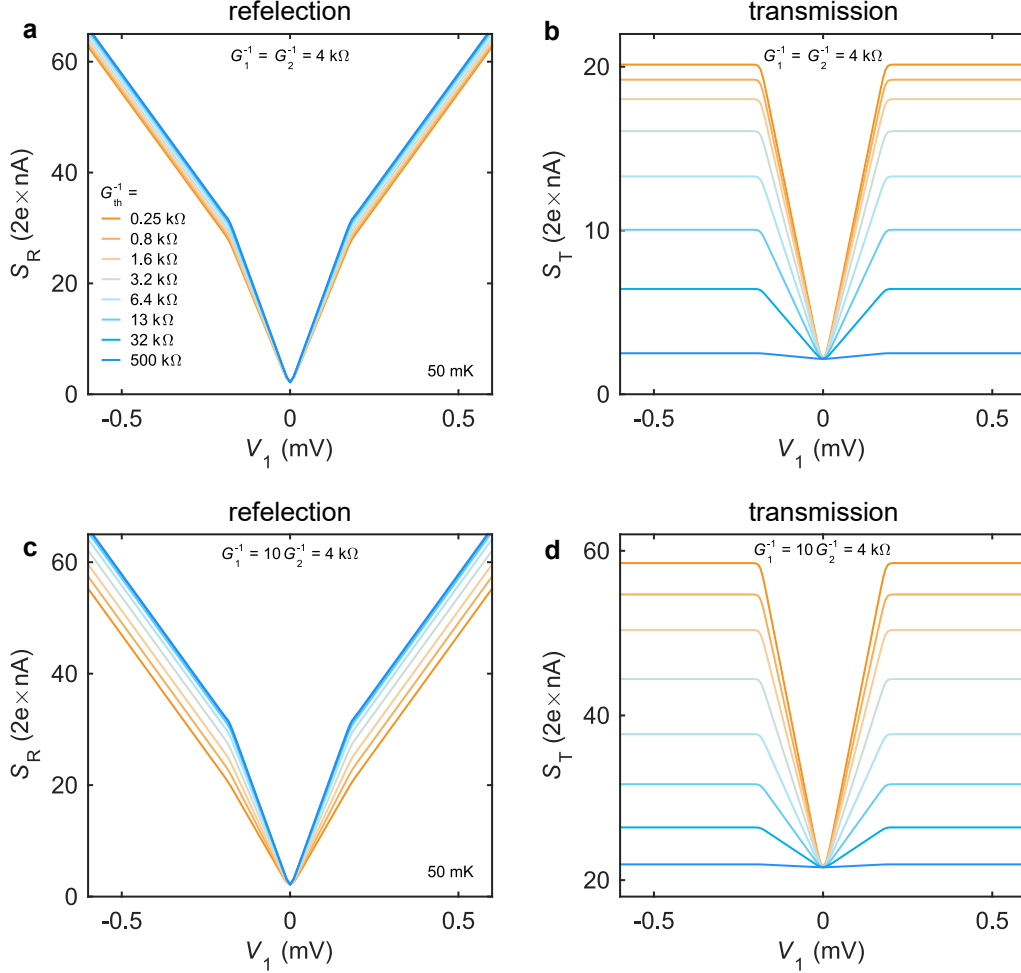


FIG. S12. **Analytical model: results.** (a) - (b) Calculated shot noise in reflection and transmission configurations for $G_1 = G_2$ and various G_{th} . (c) - (d) Calculated shot noise in reflection and transmission configurations for $G_2 = 10G_1$ and various G_{th} .

Calculated with (S5) reflected and transmitted shot noise are plotted in fig.S12. For clarity, we consider a case of the perfect interface $r = 0$ in two limits of symmetric $G_1 = G_2$ (a, b) and highly asymmetric $G_1 = 0.1G_2$ (c, d) NSN device. Here we vary G_{th} which is responsible for the heat transmission between two adjacent NS junctions.

For pinched off or extra-long middle section of NSN device $G_{th} \ll G_{1/2}$, two NS junctions are almost decoupled from each other and the transmitted signal in fig. S12 b, d is negligible. At the same time, the reflected noise is following the well-known $e^* = 2e \rightarrow e$ crossover for

diffusive NS junctions [S1] that means a complete sub-gap reflection of the heat flux from S terminal. Increasing G_{th} we allow some heat transmission towards the right N terminal which results in the reduced sub-gap effective charge $e^* < 2e$ (slope) of the reflected noise. Particularly for the asymmetric device, effective charge approaches a single value $e^* \rightarrow e$ as $G_{\text{th}}, G_2 \gg G_1$ in fig. S12c. This is expected since S terminal in this case is effectively shorted with the right N terminal which serves as a heat sink for sub-gap quasiparticles.

The lost portion of the reflected heat flux is evident from the transmitted signal in fig. S12b, d which increases with increasing G_{th} at given bias voltage for both symmetric and asymmetric NSN junctions. Being the strong function of thermal conductance, the non-local noise is suitable for accurate determination of G_{th} .

Noise vs. Resistive thermometry

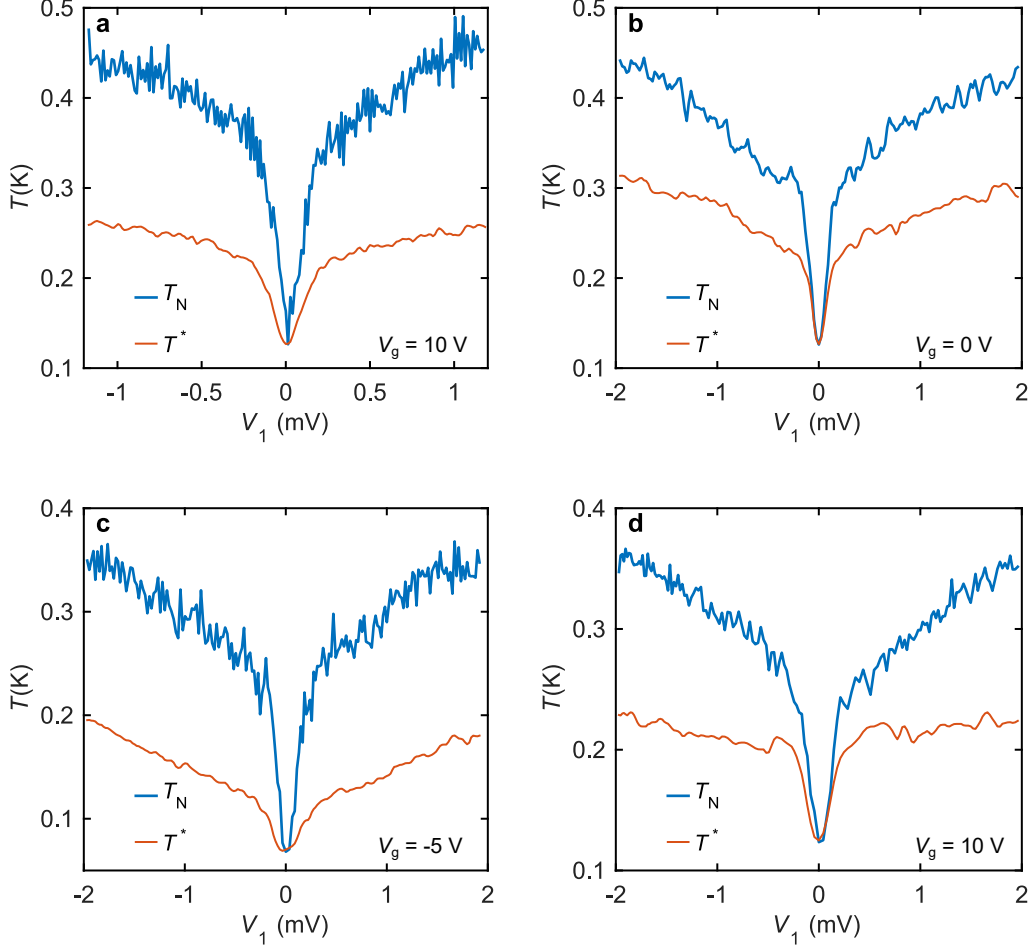


FIG. S13. **Comparison of the non-local noise thermometry and resistive thermometry.**

(a) - (b) Measured noise and effective temperature of the floating NS junction (NSN - II device) at different back - gate voltages. Zero-bias thermometry underestimates noise one by the factor of ~ 2 .

In this section we highlight the difference between noise thermometry and resistive thermometry approaches.

To describe numerically the resistive thermometry, we consider NS junction as a two-terminal coherent quasi-1D conductor with n channels and energy-dependent diagonal transmission coefficients $Tr_i(\varepsilon)$ connecting two reservoirs with temperatures T_L and T_R . We now determine the linear response conductance G_1 in such a system, where a temperature bias

across the conductor might be present.

If a small voltage bias dV is applied across the conductor, the linear-response current through the nanowire dI is [S3]:

$$dI = \frac{2e}{h} \sum_i^n \int Tr_i(\varepsilon) \left[f\left(\varepsilon - \frac{edV}{2}, T_R\right) - f\left(\varepsilon + \frac{edV}{2}, T_L\right) \right] d\varepsilon, \quad (\text{S11})$$

where $f(\varepsilon, T)$ is the equilibrium Fermi-Dirac distribution at temperature T . We note, that the conductance temperature dependence in this model is fully enclosed in the energy dependence of $Tr_i(\varepsilon)$. Now we transform this equation by taking out the small bias from the distribution functions and separating the sum:

$$dI = \frac{2e}{h} \int \left[\sum_i^n Tr_i(\varepsilon) \right] \left[\frac{\partial f(\varepsilon, T_R)}{\partial \varepsilon} \left(-\frac{edV}{2} \right) - \frac{\partial f(\varepsilon, T_L)}{\partial \varepsilon} \left(\frac{edV}{2} \right) \right] d\varepsilon, \quad (\text{S12})$$

which leads to the linear response conductance $G_{1,\text{non-eq}}$ in form:

$$G_1 = \partial I / \partial V = -\frac{2e^2}{h} \frac{1}{2} \int \left[\sum_i^n Tr_i(\varepsilon) \right] \left[\frac{\partial f(\varepsilon, T_R)}{\partial \varepsilon} + \frac{\partial f(\varepsilon, T_L)}{\partial \varepsilon} \right] d\varepsilon = \frac{G_1(T_R) + G_1(T_L)}{2}. \quad (\text{S13})$$

where $G_1(T)$ is the ordinary equilibrium conductance which can be measured by varying the bath temperature. The (S13) clearly demonstrates, that the temperature, measured via resistive thermometry T^* in the main text obeys a relation:

$$G_1(T^*) = \frac{G_1(T_R) + G_1(T_L)}{2}, \quad (\text{S14})$$

We note, that this result is only valid for the case of equilibrium distribution functions at both nanowire terminals. For the triple-step distribution expected for S terminal in our experiment, the conductance depends on the exact form of $Tr_i(\varepsilon)$.

We now compare this result for T^* with the expected noise temperature T_N when one terminal has significantly higher temperature ($T_R \gg T_L$). For this case T_N can be expressed in form $T_N = \alpha T_R$, with coefficient α depending on the shape of distribution function at the terminal [S4]. For the double-step distribution $\alpha = 2/3$, while in the case of equilibrium distribution $\alpha = (1 + \ln(2))/2 \approx 0.56$.

Neglecting the non-linearity of $G_1(T)$, which is present in experiment (see supplemental fig. S9b), we obtain that the relation $T_N \approx 4/3 T^*$.

In experiment, however, the discrepancy between T_N and T^* is more prominent with $T_N - T_{\text{bath}} \approx 2(T^* - T_{\text{bath}})$ (see supplemental fig. S13). Apart from the discussed earlier effect of the non-equilibrium distribution on G_1 , this inconsistency might be related to the dephasing being present in nanowire. Such dephasing may effectively break the nanowire into several coherent section, with possibly different signs of temperature dependence, leading to a further dampening of T^* compared to T_N .

Non-local voltage generated by temperature bias

In order to describe the symmetric component of the non-local I - V s presented in Fig. 4d of the main text we consider a thermoelectric generation of voltage. In the Landauer-Büttiker formalism, the conversion of the temperature bias to electric current is a result of the energy dependence of the eigen-channel transparencies $Tr_i(\varepsilon)$. Thermoelectric current generated in a short-circuited conductor can be written as:

$$I_{\text{TE}} = \frac{2e}{h} \sum_i^n \int Tr_i(\varepsilon) [f(\varepsilon, T_R) - f(\varepsilon, T_L)] d\varepsilon \approx \frac{2e}{h} \sum_i^n Tr'_i \int \varepsilon [f(\varepsilon, T_R) - f(\varepsilon, T_L)] d\varepsilon, \quad (\text{S15})$$

where the quasiparticle energy ε is measured with respect to the chemical potential that is the same for the right and left leads of the conductor. Note that in this equation we approximated the energy dependence $Tr_i(\varepsilon)$ with the lowest order non-vanishing term $Tr_i(\varepsilon) = Tr_i(0) + Tr'_i \varepsilon$, where $Tr'_i \equiv dTr_i(\varepsilon)/d\varepsilon|_{\varepsilon=0}$. It is straightforward to see that eq. (S15) results in a parabolic T-dependence of I_{TE} :

$$I_{\text{TE}} \approx \frac{\pi^2 k_B^2}{6} \frac{2e}{h} \sum_i^n Tr'_i [T_R^2 - T_L^2]. \quad (\text{S16})$$

Measured thermoelectric voltage that builds up on a floating conductor is simply $V_{\text{TE}} = -I_{\text{TE}} G_0^{-1}$, where $G_0 = 2e^2/h \sum_i^n Tr_i(0)$ is the linear-response conductance. For a small temperature difference $\Delta T \equiv T_R - T_L \ll T$, the eq. (S16) can be written as:

$$V_{\text{TE}} \approx (S/T) T \Delta T, \text{ where } S/T = -\frac{\pi^2 k_B^2}{3e} \sum_i^n Tr'_i \left[\sum_i^n Tr_i \right]^{-1}. \quad (\text{S17})$$

In other words, in this approximation the thermoelectric response is fully characterized by the T-independent Seebeck parameter S/T . With this notation we obtain the expression for arbitrary thermal biases on the conductor:

$$V_{\text{TE}} \approx (S/T) \frac{T_R^2 - T_L^2}{2}, \quad (\text{S18})$$

that is used to fit the data for V_2^{symm} in Fig. 4d of the main text.

Critical Temperature of Al contacts

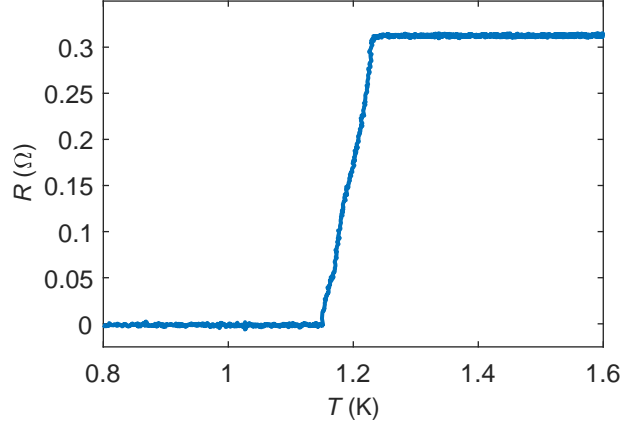


FIG. S14. **Superconducting critical temperature of the Al-film.** The resistance of a four-terminal Al strip, deposited via the same process, as the one used in the fabrication of the samples, featured in the main text.

The temperature dependence of superconducting Al, deposited via the same process as described in "Device Fabrication" was performed separately on the four-terminal Al strips, incorporated in the samples studied in [S5]. Here we present raw data (see Fig. S14), which leads to the estimate $T_c = 1.20 \pm 0.03$ K, based on the position of the middle of transition.

Device fabrication

InAs nanowires grown by molecular beam epitaxy on Si substrate [S6] are ultrasonicated in isopropyl alcohol. Nanowires are drop casted on Si/SiO₂ (300 nm) substrates [S7] with preliminary defined alignment marks. For superconducting contacts conventional electron beam lithography (EBL) followed by e-beam deposition of Al (150 nm) is utilized. To obtain the ohmic contacts, in-situ Ar ion milling is performed before Al deposition in a chamber with a base pressure below 10^{-7} mbar. Normal metal contacts are fabricated in two different ways (different device batches): magnetron sputtering or e-beam deposition. For sputtering (NS and NSN - I devices) in-situ Ar plasma etching is followed by sputtering of Ti/Au (5 nm/200 nm). Normal metal contacts Ti/Au (5 nm/150 nm) in device NSN - II are deposited in the same way as superconducting ones.

-
- [S1] K. E. Nagaev and M. Büttiker, Semiclassical theory of shot noise in disordered superconductor–normal-metal contacts, *Phys. Rev. B* **63**, 081301 (2001).
 - [S2] K. Nagaev, On the shot noise in dirty metal contacts, *Physics Letters A* **169**, 103 (1992).
 - [S3] Y. Blanter and M. Büttiker, Shot noise in mesoscopic conductors, *Physics Reports* **336**, 1 (2000).
 - [S4] E. S. Tikhonov, D. V. Shovkun, D. Ercolani, F. Rossella, M. Rocci, L. Sorba, S. Roddaro, and V. S. Khrapai, Local noise in a diffusive conductor, *Scientific Reports* **6**, 30621 EP (2016), article.
 - [S5] A. V. Bubis, A. O. Denisov, S. U. Piatrusha, I. E. Batov, V. S. Khrapai, J. Becker, J. Treu, D. Ruhstorfer, and G. Koblmüller, Proximity effect and interface transparency in al/InAs-nanowire/al diffusive junctions, *Semiconductor Science and Technology* **32**, 094007 (2017).
 - [S6] S. Hertenberger, D. Rudolph, M. Bichler, J. J. Finley, G. Abstreiter, and G. Koblmüller, Growth kinetics in position-controlled and catalyst-free InAs nanowire arrays on si(111) grown by selective area molecular beam epitaxy, *Journal of Applied Physics* **108**, 114316 (2010).
 - [S7] J. Becker, S. Morkötter, J. Treu, M. Sonner, M. Speckbacher, M. Döblinger, G. Abstreiter, J. J. Finley, and G. Koblmüller, Carrier trapping and activation at short-period wurtzite/zinc-blende stacking sequences in polytypic inas nanowires, *Phys. Rev. B* **97**, 115306 (2018).